

1 **Bayesian performance evaluation of evapotranspiration models based on eddy**  
2 **covariance systems in the arid region**

3 Guoxiao Wei <sup>1,2</sup>, Xiaoying Zhang <sup>3,\*</sup>, Ming Ye <sup>4</sup>, Ning Yue <sup>1,2</sup>, Fei Kan <sup>1,2</sup>

4 <sup>1</sup> Key Laboratory of Western China's Environmental System (Ministry of Education), Lanzhou University,  
5 China, 730000

6 <sup>2</sup> School of Earth and Environmental Sciences, Lanzhou University, China, 730000

7 <sup>3</sup> Construct Engineering College, Jilin University, China, 130400

8 <sup>4</sup> Department of Earth, Ocean, and Atmospheric Science, Florida State University, USA, 32306

9 \* Corresponding author: xiaoyingzh@jlu.edu.cn.

10 **Abstract**

11 Evapotranspiration (ET) is a major component of the land surface process involved in energy fluxes and energy  
12 balance, especially in the hydrological cycle of agricultural ecosystems. While many models have been  
13 developed as powerful tools to simulate ET, there is no agreement on which model best describing the loss of  
14 water to the atmosphere. This study focuses on two aspects, evaluating the performance of four widely used ET  
15 models, and identifying parameters, as well the physical mechanisms that have significant impacts on the model  
16 performance. The four tested models are Shuttleworth Wallace (SW) model, Penman-Monteith (PM) model,  
17 Priestley-Taylor and Flint-Childs (PT-FC) model, and Advection-Aridity (AA) model. By incorporating the  
18 mathematically rigorous thermodynamic integration algorithm, the Bayesian model evidence (BME) approach is  
19 adopted to select the optimal model with half-hourly ET observations obtained at a spring maize field in an arid  
20 region. Our results reveal that SW has the best performance and the extinction coefficient is not merely  
21 partitioning the total available energy into the canopy and surface, but also including the energy imbalance  
22 correction. The extinction coefficient is well constrained in the SW model and poorly constrained in the PM  
23 model, but not considered in PT-FC and AA models. This is one of the main reasons that the SW model  
24 outperforming the other models. Meanwhile, the good fitting of SW model to observations can counterbalance  
25 its higher complexity. In addition, the detailed analysis of the discrepancies between observations and model  
26 simulations during the crop growth season indicate that explicit treatment of energy imbalance and energy  
27 interaction will be the primary way to further improve ET model performance.

28 **Keywords:** Bayesian analysis; ET models; Eddy covariance; Model performance; Extinction coefficient

## 29 **1. Introduction**

30 Surface energy fluxes are an important component of Earth's global energy budget and a primary  
31 determinant of surface climate. Evapotranspiration (ET), as a major energy flux process for energy balance,  
32 accounts for about 60-65% of the average precipitation over the surface of the Earth (Brutsaert, 2005). In  
33 agricultural ecosystems, more than 90% of the total water losses are due to ET (Morison et al., 2008). Therefore,  
34 robust ET estimation is crucial to a wide range of problems in hydrology, ecology, and global climate change  
35 (Xu and Singh, 1998). In practice, much of our understanding of how land surface processes and vegetation  
36 affect weather and climate is based on numerical modeling of surface energy fluxes and the  
37 atmospherically-coupled hydrological cycle (Bonan, 2008). Several models are commonly used in agricultural  
38 systems to evaluate ET. The Penman-Monteith (PM) and Shuttleworth-Wallace (SW) models are physically  
39 sound and rigorous (Zhu et al., 2013), and thus widely used to simulate ET for seasonally varied vegetations.  
40 The models consider the relationships between net radiation, all kinds of heat flux (such as latent heat, sensible  
41 heat, and heat from soil and canopy), and surface temperature. The Priestley-Taylor and Flint-Childs (PT-FC)  
42 model (based on radiation) and the advection-aridity (AA) model (based on meteorological variables) have also  
43 been widely used because they only require a small number of ground-based measurements to set up the models  
44 (Ershadi et al., 2014).

45 Comparing the performance of the competing ET models and evaluating and understanding the  
46 discrepancies between simulations of the models and corresponding observed surface-atmosphere water flux are  
47 remain challenging problems (Legates, 1999). Both non-Bayesian analysis (Szilagyi and Jozsa, 2008; Vinukollu  
48 et al., 2011; Li et al., 2013; Ershadi et al., 2015) and Bayesian analysis have been used to evaluate the  
49 performance of ET models (Zhu et al., 2014; Chen et al., 2015; Liu et al., 2016; Zhang et al., 2017; Elshall et al.,  
50 2018; Samani et al., 2018; Zeng et al., 2018) . Li et al. (2013) compared the ET simulations of the PM, SW and  
51 adjusted SW models under film-mulching conditions of maize growth in an arid region of China. They found  
52 that the half-hourly ET was overestimated by 17% by the SW model. In contrast, the PM and adjusted SW  
53 models underestimated the daily ET by 6% and 2%, respectively. Therefore, the performances of PM and  
54 adjusted SW models are better than that of the SW model in their case study. Ershadi et al. (2014) evaluated the  
55 surface energy balance system (SEBS), PM, PT-JPL (a modified Priestley-Taylor model) and AA models.  
56 Based on the average value of EF and RMSE, the model ranking from worst to best was AA, PM, SEBS, and

57 PT-JPL. Ershadi et al. (2015) also compared the response of the models to different formulations of  
58 aerodynamic and surface resistances with global FLUXNET data. Their results showed considerable variability  
59 in model performance among and within biome types. Currently, ET model selection and comparison have been  
60 still conducted using traditional error metrics. It is known that error metrics are not adequate to provide a  
61 reasonable result of model ranking for disregarding model complexity (Marshall et al., 2005; Samani et al.,  
62 2018). The focus of this study is to use a Bayesian approach to evaluate the performance of the PM, SW, PT-FC,  
63 and AA models, which is a novelty contribution of this study. In ET models, the land surface energy system is  
64 governed by presumably infinite-dimensional physics. However, considering the ET models as  
65 finite-dimensional can be more precisely by covering all relevant relations. Therefore, employing consistent  
66 criteria for model selection might be justified when the aim is to better understand the processes involved (H öge  
67 et al., 2018). When using consistent model selection, Bayesian model evidence (BME), also known as marginal  
68 likelihood, measures the average fit of model simulations to their corresponding observations over a model's  
69 prior parameter space. This feature enables BME to consider model complexity (in terms of the number of  
70 model parameters) for model performance evaluation. When comparing several alternative conceptual models,  
71 the model with the largest marginal likelihood is selected as the best model (Lartillot and Philippe, 2006). BME  
72 can thus be used for evaluating the model fit (over the parameter space) and for comparing alternative models.  
73 In previous studies, the Bayesian information criterion (BIC; Schwarz, 1978) and the Kashyap information  
74 criterion (KIC; Kashyap, 1982) have been used to approximate BME by using maximum likelihood theories to  
75 reduce the computational cost of evaluating BME (Ye et al., 2004). However, these approximations have  
76 theoretical and computational limitations (Ye et al., 2008; Xie et al., 2011; Sch öniger et al., 2014), and a  
77 numerical evaluation (not a likelihood approximation) of BME is necessary, especially for complex models  
78 (Lartillot and Philippe, 2006). Lartillot and Philippe (2006) advocated the use of thermodynamic integration (TI)  
79 for estimating BME, also known as path sampling (Gelman and Meng, 1998; Neal, 2000), in order to avoid  
80 sampling solely in the prior or posterior parameter space. TI uses samples that are systematically generated from  
81 the prior to the posterior parameter space by conducting path sampling with several discrete power coefficient  
82 values (Liu et al., 2016). It is numerically accurate than the generally used harmonic mean method (Xie et al.,  
83 2011).

84 Most applications of Bayesian methods have focused on the calibration of individual models, while the  
85 comparison of alternative models continues to be performed using traditional error metrics. More generally,

86 Bayesian approaches to model calibration, comparison, and analysis have been used far less used in the  
87 evaluation of ET models than in other areas of environmental science. In this study, the Bayesian approach is  
88 used to calibrate and evaluate the four ET models (PM, SW, PT-FC, and AA) based on an experiment over a  
89 spring maize field in an arid area of northwest China, from 3 June to 27 September 2014. The objectives of the  
90 study are as follows: (1) to calibrate ET model parameters using the DiffereRential Evolution Adaptive Metropolis  
91 (DREAM) algorithm (Vrugt et al., 2008, 2009); (2) to identify which parameters had a greater impact on the  
92 model performance and to explain why the selected optimal model performed best; (3) to evaluate the  
93 performance of the models using traditional error metrics and BME; and (4) to analyze discrepancies between  
94 model simulations and observation data in order to better understand model performance and identify ways to  
95 improve these models. We expect that the study will not only boost the development of model parameterization  
96 and model selection but also contribute to the improvement of the ET models.

## 97 **2. Data and methodology**

### 98 **2.1. Description of the study area**

99 The experiment of maize growth was conducted at Daman Superstation, located in Zhangye City, Gansu  
100 province, northwest China. Daman Oasis is located in the middle Heihe River basin, which is the second largest  
101 inland river basin in the arid region of northwest China. The midstream area of the Heihe River basin is  
102 characterized by oases with irrigated agriculture and is a region that consumes a large amount of water for both  
103 domestic and agricultural uses. The annual average precipitation and temperature are 125 mm and 7.2 °C  
104 (1960–2000), respectively. The annual accumulated temperature (>10 °C) is 3,234 °C, and the annual average  
105 potential evaporation is about 2,290 mm. The average annual duration of sunshine is 3,106 h with 148 frost-free  
106 days. The predominant soil type is silty-clay loam and the depth of the frozen layer is about 143 mm. The study  
107 area is a typical irrigated agricultural region, and the major source of water is snowmelt from the Qilian  
108 Mountains. Maize and spring wheat are the principal crops grown in the region. Maize is generally sown in late  
109 April and harvested in mid-September and is planted with a row spacing of 40 cm and a plant spacing of 30 cm.  
110 The plant density is about 66,000 plants per hectare in the study area.

### 111 **2.2. Measurements and data processing**

112 Our data were collected from the field observation systems of the Heihe Watershed Allied Telemetry

113 Experimental Research (HiWATER) project as described in Li et al (2013). The observation period was from  
 114 DOY (day of the year) 154 to DOY 270 in 2014. An open-path eddy covariance (EC) system was installed in a  
 115 maize field, with the sensors at a height of 4.5 m. Maize is the main crop in the study region, and thus covers  
 116 sufficient planting area to set the EC measurements. The EC data was logged at a frequency of 10 Hz and then  
 117 processed with an average time interval of 30 min. Sensible and latent heat fluxes were computed by the EC  
 118 approach of Baldocchi (2003). Flux data measured by EC were controlled by traditional methods, including  
 119 three-dimensional rotation (Aubinet et al., 2000), Webb-Penman-Leuning (WPL ) density fluctuation correction  
 120 (Webb et al., 1980), frequency response correction (Xu et al., 2014), and spurious data removal caused by  
 121 rainfall, water condensation, and system failure. About 85% of the energy balance closure was observed in the  
 122 EC data (Liu et al., 2011).

123 Standard hydro-meteorological variables, including rainfall, air temperature, wind speed, and wind  
 124 direction, were continuously measured at the heights of 3, 5, 10, 15, 20, 30 and 40 m above the ground. Soil  
 125 temperature and moisture were measured at heights of 2, 4, 10, 20, 40, 80, 120 and 160 cm. Photosynthetically  
 126 active radiation was measured at a height of 12 m. Net radiation, including downward, upward and longwave  
 127 radiation, was measured by a four-component net radiometer. An infrared thermometer was installed at a height  
 128 of 12 m. Leaf Area Index (LAI) was measured approximately every 10 days during the growing season.

### 129 **2.3. Model description**

130 In this section, we summarize the mathematical definitions forming the basis of each of the four models.  
 131 Appendix A contains a summary of the names and physical meanings of the model parameters.

#### 132 **2.3.1 Penman-Monteith (PM) model**

133 The PM model can be formulated in the following way (Monteith, 1965):

$$134 \quad \lambda E = \frac{\varepsilon A + (\rho C_p / \gamma) D_a g_a}{\varepsilon + 1 + g_a / g_s} \quad (1)$$

135 where  $\varepsilon = \Delta / \gamma$ ; and  $A$  is defined to be  $A = R_n - G$ .

136 In the present study,  $g_a$  is parameterized in the way suggested by Leuning (2008) and  $g_s$  is defined as:

$$g_s = g_s^c \left[ \frac{1 + \frac{\tau g_a}{(\varepsilon + 1) g_s^c} \left[ f - \frac{(\varepsilon + 1)(1 - f) g_s^c}{g_a} \right] + \frac{g_a}{\varepsilon g_i}}{1 - \tau \left[ f - \frac{(\varepsilon + 1)(1 - f) g_s^c}{g_a} \right] + \frac{g_a}{\varepsilon g_i}} \right] \quad (2)$$

where  $1 - \tau$  and  $\tau$  are the fractions of the total available energy absorbed by the canopy and by the soil, and  $\tau = \exp(-K_d LAI)$ , and  $g_i$  and  $g_s^c$  are defined in equations (3) and (4), respectively (Monteith, 1965):

$$g_i = \frac{A}{(\rho C_p / \gamma) D_a} \quad (3)$$

$$g_s^c = \frac{g_{\max}}{K_q} \ln \left[ \frac{Q_h + Q_{50}}{Q_h \exp(-K_q LAI) + Q_{50}} \right] \left[ \frac{1}{1 + D_a / D_{50}} \right] f(\theta) \quad (4)$$

where  $f(\theta)$  represents water stress and is expressed as:

$$f(\theta) = \begin{cases} 1 & \theta > \theta_a \\ \frac{\theta - \theta_b}{\theta_a - \theta_b} & \theta_b < \theta < \theta_a \\ 0 & \theta < \theta_b \end{cases} \quad (5)$$

and  $\theta_a$  is set as  $\theta_a = 0.75 \theta_b$ . Aerodynamic conductance  $g_a$  is calculated as:

$$g_a = \frac{k^2 u_m}{\ln[(z_m - d)/z_{0m}] \ln[(z_m - d)/z_{0v}]} \quad (6)$$

where the quantities  $d$ ,  $z_{0m}$  and  $z_{0v}$  are calculated using  $d = 2h/3$ ,  $z_{0m} = 0.123h$  and  $z_{0v} = 0.1z_{0m}$  (Allen 1998).

### 2.3.2. Shuttleworth-Wallace (SW) model

The SW model comprises a one-dimensional model of plant transpiration and a one-dimensional model of soil evaporation. The two terms are calculated by the following equations:

$$\lambda ET = \lambda E + \lambda T = C_s ET_s + C_c ET_c \quad (7)$$

$$ET_s = \frac{\Delta A + \{ \rho C_p (e_s - e_a) - \Delta r_a^s (A - A_s) \}}{\Delta + \gamma \{ 1 + r_s^s / (r_a^a + r_a^s) \}} \quad (8)$$

$$152 \quad ET_c = \frac{\Delta A + \{\rho C_p (e_s - e_a) - \Delta r_a^c A_s\} / (r_a^a + r_a^c)}{\Delta + \gamma \{1 + r_s^c / (r_a^a + r_a^c)\}} \quad (9)$$

153 where the available energy input above the soil surface is defined as  $A_s = R_{ns} - G$ .

154  $R_{ns}$  can be calculated using the Beer's law relationship:

$$155 \quad R_{ns} = R_n \exp(-K_a LAI) \quad (10)$$

156 The coefficients  $C_s$  and  $C_c$  are obtained as follows:

$$157 \quad C_s = \{1 + R_s R_a / R_c (R_s + R_a)\}^{-1} \quad (11)$$

$$158 \quad C_c = \{1 + R_c R_a / R_s (R_c + R_a)\}^{-1} \quad (12)$$

159 where

$$160 \quad R_a = (\Delta + \gamma) r_a^a \quad (13)$$

$$161 \quad R_s = (\Delta + \gamma) r_a^s + \gamma r_s^s \quad (14)$$

$$162 \quad R_c = (\Delta + \gamma) r_a^c + \gamma r_s^c \quad (15)$$

163 Soil surface resistance is expressed as:

$$164 \quad r_s^s = \exp(b_1 - b_2 \frac{\theta}{\theta_s}) \quad (16)$$

165 In this study, we consider the reciprocal of bulk stomatal resistance, known as canopy conductance. The  
 166 calculation of  $g_s^c$  is the same as in the PM model. The two aerodynamic resistances ( $r_a^a$  and  $r_a^s$ ) and the  
 167 boundary layer resistance ( $r_a^c$ ) are modeled following the approach proposed by Shuttleworth and Gurney  
 168 (1990).

### 169 2.3.3. Priestley-Taylor and Flint-Childs (PT-FC) model

170 The Priestley-Taylor model (Priestley and Taylor, 1972) was introduced to estimate evaporation from an

171 extensive wet surface under conditions of minimum advection (Stannard, 1993; Sumner and Jacobs, 2005). The  
 172 ET is expressed as:

$$173 \quad \lambda ET = \alpha_{PT} \frac{\Delta}{\Delta + \gamma} (R_n - G) \quad (17)$$

174 where  $\alpha_{PT}$  is a unitless coefficient. The Priestley-Taylor model was modified by Flint and Childs (1991) in order  
 175 to scale the Priestley-Taylor potential ET to actual ET for nonpotential conditions (hereafter the PT-FC model):

$$176 \quad \lambda ET = \alpha \frac{\Delta}{\Delta + \gamma} (R_n - G) \quad (18)$$

177 where  $\alpha$  is as a function of the environmental variables, which could be related to any process that limits ET  
 178 (e.g., soil hydraulic resistance, aerodynamic resistance, stomatal resistance); however, only soil moisture status  
 179 was considered to simplify ET estimation in the PT-FC model (Flint and Childs, 1991). In this model,  $\alpha$  is  
 180 defined as:

$$181 \quad \alpha = \beta_1 [1 - \exp(-\beta_2 \Theta)] \quad (19)$$

$$182 \quad \text{where } \Theta = \frac{\theta - \theta_r}{\theta_s - \theta_r}.$$

#### 183 **2.3.4. Advection-aridity (AA) model**

184 The AA model was first proposed by Brutsaert and Stricker (1979) and further improved by Parlange and  
 185 Katul (1992). The model relies on the feedback between actual ( $\lambda ET$ ) and potential  $ET$ , which assumes that  
 186 actual potential  $ET$  should converge to wet surface  $ET$  at wet surface conditions. Its general form is:

$$187 \quad \lambda ET = (2\alpha_{PT} - 1) \frac{\Delta}{\Delta + \gamma} (R_n - G) - \frac{\gamma}{\Delta + \gamma} \frac{\rho(q^* - q)}{r_a} \quad (20)$$

188 where  $\alpha_{PT}$  is the Priestley-Taylor coefficient, usually taken as 1.26 (Priestley and Taylor, 1972); and  $r_a$  is similar  
 189 to that used for the Penman-Monteith model (Brutsaert and Stricker, 1979; Brutsaert, 2005; Ershadi et al., 2014).  
 190 This model is based mainly on meteorological variables and does not require any information related to soil  
 191 moisture, canopy resistance or other measures of aridity (Ershadi et al., 2014). In this study, we changed  $\alpha_{PT}$  to  $\alpha$ ,



192 which is calculated using the same equation as in the PT-FC model.

## 193 **2.4 BME Estimation**

194 The Bayesian model evidence (BME) of a model,  $M$ , is defined as (Schöniger et al., 2014):

$$195 \quad \text{BME} = p(\mathbf{D}|M) = \int p(\mathbf{D}|\boldsymbol{\theta}, M) p(\boldsymbol{\theta}|M) d\boldsymbol{\theta} \quad (21)$$

196 where  $\mathbf{D}$  is observed or estimated data,  $\boldsymbol{\theta}$  is the vector of parameters associated with model  $M$ ,  $p(\boldsymbol{\theta}|M)$  is

197 the prior density of  $\boldsymbol{\theta}$  under model  $M$ ,  $p(\mathbf{D}|\boldsymbol{\theta}, M)$  is the joint likelihood of model  $M$  and its parameters  $\boldsymbol{\theta}$ .

198 Estimating BME using power posterior estimators such as thermodynamic integration (TI) (Lartillot and

199 Philippe, 2006) depends mainly on the calculation of the marginal likelihood  $p(\mathbf{D}|M)$ . The main idea of power

200 posterior sampling is to define a path that links the prior to the unnormalized posterior. Thus, using an

201 unnormalized power posterior density

$$202 \quad q_\beta(\boldsymbol{\theta}) = p(\mathbf{D}|\boldsymbol{\theta}, M)^\beta p(\boldsymbol{\theta}|M) \quad (22)$$

203 the power coefficient  $\beta \in [0, 1]$  is a scalar parameter for discretizing a continuous and differentiable path

204 linking two unnormalized power posterior densities. The unnormalized power posterior density  $q_\beta(\boldsymbol{\theta})$  in

205 Equation (22) uses the normalizing constant  $Z_\beta$  to yield the normalized power posterior density:

$$206 \quad p_\beta(\boldsymbol{\theta}) = \frac{q_\beta(\boldsymbol{\theta})}{Z_\beta} \quad (23)$$

207 such that

$$208 \quad Z_\beta = \int q_\beta(\boldsymbol{\theta}) d\boldsymbol{\theta} \quad (24)$$

209 The above integral takes a simplified form by the potential:

$$210 \quad U(\boldsymbol{\theta}) = \frac{\partial \ln q_\beta(\boldsymbol{\theta})}{\partial \beta} \quad (25)$$

211 thus, the integral can be directly estimated by the following way:

$$212 \quad p(\mathbf{D}|M) = \frac{Z_1}{Z_0} = \exp\left\{\int_0^1 E_\theta[\ln p(\mathbf{D}|\boldsymbol{\theta}, M)] d\beta\right\} \quad (26)$$

213 The one-dimensional integral with respect to  $\beta$  is evaluated by using numerical methods by discretizing  $\beta$  into a  
 214 set of  $\beta_k$ . Since there is no theoretical method for selecting  $\beta_k$  values (Liu et al., 2016), we determined these  
 215 values using an empirical but straightforward method. Following Xie et al. (2011), a schedule of the power  
 216 posterior coefficients  $\beta_k$  is generated by

$$217 \quad \beta_k = (k / K)^{1/\varepsilon} \quad (27)$$

218 for  $k=0, 1, 2, \dots, K$ . Using  $\varepsilon = 0.3$  and  $K = 20$  is a reasonable initial choice. By using the trapezoidal rule of  
 219 numerical inregration, equation (26) is evaluated via

$$220 \quad p(\mathbf{D} | M) = \exp\left(\int_0^1 y_\beta d\beta\right) = \exp\left(\sum_{k=0}^K r_{TI,k}\right) \quad (28)$$

221 such that

$$222 \quad r_{TI,k} = (\beta_k - \beta_{k-1}) \left[ \frac{y_k - y_{k-1}}{2} \right] \quad (29)$$

223 and

$$224 \quad y_k = E_\beta[\log p(\mathbf{D} | \boldsymbol{\theta}_k, M)] = \frac{1}{n} \sum_{i=1}^n \log p(\mathbf{D} | \boldsymbol{\theta}_{k,i}, M) \quad (30)$$

225 where  $n$  is the number of random samples of  $\boldsymbol{\theta}_k$  corresponding to  $\beta_k$ , and  $\boldsymbol{\theta}_{k,i}$  is the  $i$ -th sample.

226 The random samples,  $\boldsymbol{\theta}_{k,i}$ , are drawn by using the MCMC method implemented in the DREAM code. See

227 Appendix B for further details on Bayesian inference and the DREAM algorithm. In the DREAM-based

228 calculation, the Metropolis acceptance ratio is  $\alpha_k = \min\left(1, [\alpha_{k, power-posterior} \alpha_{k, prior}]\right)$  with the power

229 posterior ratio given by  $\alpha_{k, power-posterior} = \left(\alpha_{k, posterior}\right)^{\beta_k}$ . The prior probability ratio

230  $\alpha_{k, prior} = \Pr(\boldsymbol{\theta}_{k, new} | M) / \Pr(\boldsymbol{\theta}_{k, old} | M)$  is the ratio of the probability of the newly proposed sample

231  $\boldsymbol{\theta}_{k, new}$  and the probability of the previously accepted sample  $\boldsymbol{\theta}_{k, old}$ . The posterior probability ratio

232  $\alpha_{k,posterior} = L(\mathbf{D} | \boldsymbol{\theta}_{k,new}, M) / L(\mathbf{D} | \boldsymbol{\theta}_{k,old}, M)$  is the likelihood ratio of samples  $\boldsymbol{\theta}_{k,new}$  and  $\boldsymbol{\theta}_{k,old}$ , and

233  $\beta_k$  is the power posterior coefficient. Thus, to use the DREAM algorithm to sample any power posterior

234 distribution, the regular Metropolis acceptance ratio  $\alpha = \min(1, [\alpha_{posterior} \alpha_{prior}])$  is changed to

235  $\alpha_k = \min(1, [\alpha_{k,power-posterior} \alpha_{k,prior}])$  in DREAM.

## 236 2.5 Traditional statistical metrics of evaluating model performance

237 The traditional error metrics for evaluating model performance include  $R^2$  and slope (correlation-based  
 238 measures), index of agreement (IA) and model efficiency (EF) (relative error measures), and the root mean  
 239 square error (RMSE) and mean bias error (MBE) (Poblete-Echeverria and Ortega-Farias, 2009). The definitions  
 240 of the listed metrics are:

$$241 \quad IA = 1 - \frac{\sum_{t=1}^n [O(t) - M(t)]^2}{\sum_{t=1}^n [ |O(t) - \overline{O(t)}| + |O(t) - \overline{M(t)}| ]^2} \quad (31)$$

$$242 \quad EF = 1 - \frac{\sum_{t=1}^n [O(t) - M(t)]^2}{\sum_{t=1}^n [O(t) - \overline{O(t)}]^2} \quad (32)$$

$$243 \quad RMSE = \sqrt{\frac{1}{n} \sum_{t=1}^n [O(t) - M(t)]^2} \quad (33)$$

$$244 \quad MBE = \frac{1}{n} \sum_{t=1}^n [O(t) - M(t)] \quad (34)$$

245 where  $O(t)$  is the observation and  $\overline{O(t)}$  is the mean observation at time  $t$ ;  $M(t)$  is the modeled value and

246  $\overline{M(t)}$  is the mean modeled value estimated by the posterior median parameter values; and  $n$  is the total number

247 of the observed values.

## 248 3. Results

### 249 3.1 Parameter estimation

250 The PM model has five parameters  $g_{max}$ ,  $D_{50}$ ,  $Q_{50}$ ,  $K_q$  and  $K_a$ ; the SW model has seven parameters – the five  
 251 used in the PM model and parameters  $b_1$  and  $b_2$ . The PT-FC and AA models each include two parameters,  
 252 denoted by  $\beta_1$  and  $\beta_2$  (Table 1). The prior probability density of each parameter is specified as an uniform  
 253 distribution with the ranges listed in Table 1. A total of 50,000 realizations were generated with the DREAM  
 254 algorithm, which was used to estimate the posterior probability density function of each parameter with the  
 255 calibration period data from DOY 154 to DOY 202. In the calculations, the chain number,  $N$ , was equal to the  
 256 number of parameters in the associated model. Therefore,  $N$  is equal to 5, 7, 2 and 2 for the PM, SW, PT-FC and  
 257 AA models, respectively. For each model, the first 10,000 samples were discarded as burn-in data, and the  
 258 remaining 40,000 samples were used for calibration. In total,  $40,000 \times N$  realizations were used to set up  
 259 posterior density functions for each model. To illustrate the efficiency and convergence of DREAM for the ET  
 260 models, Figure 1 shows the trace plots of the G-R statistic for each of the different parameters in the PM and  
 261 SW models using a different color. The algorithm required about 8,000 generations to make the G-R statistic  
 262 close to 1.0 for the two models. The acceptance rates for the PM and SW models were about 15.3% and 18.9%,  
 263 respectively.

264 Histograms of the DREAM-derived marginal distributions of the parameters are presented in Figure 2 and  
 265 summarized in Table 2 by Maximum Likelihood Estimates (MLEs), posterior medians and 95% probability  
 266 intervals. Figures 2a-2e, 2f-2l, 2m-2n, and 2o-2p show histograms of the PM, SW, PT-FC and AA models,  
 267 respectively. Parameter  $g_{max}$  (Fig. 2a) in the PM model, parameters  $g_{max}$ ,  $K_a$ ,  $b_2$  (Fig. 2f, 2j, 2l) in the SW model,  
 268 and parameter  $\beta_1$  (Fig. 2m) in the PT-FC model and AA model (Fig. 2o) were well constrained and occupied a  
 269 relatively small range. These parameters displayed a unimodal distribution and appeared approximately  
 270 Gaussian. In contrast, the distributions of the other parameters differed significantly from a Gaussian  
 271 distribution, as shown by the corresponding histograms. The distributions of all but one of these parameters  
 272 concentrated most of the probability mass at their upper limits. The exception was parameter  $b_1$  for the SW  
 273 model (Fig. 2k), which clearly does not follow a normal distribution with most of the mass concentrated in the  
 274 lower bounds. In contrast,  $Q_{50}$  was not only poorly constrained (Fig. 2g) but was also the upper edge-hitting  
 275 parameter in the SW model. Moreover, the corresponding distributions of the same parameter in different  
 276 models were slightly different. For example, the mean of  $g_{max}$  in the PM model ( $0.04 \text{ mm s}^{-1}$ ) was less than that  
 277 in the SW model ( $0.01 \text{ mm s}^{-1}$ ) (Fig. 2a and 2f, Table 2), except that  $D_{50}$  in the PM and SW models and  $\beta_2$  in the  
 278 PT-FC and AA models exhibited similar regions. It is interesting to observe that the distribution of  $K_a$  in PM

279 model (Figure 2e) has a truncated distribution with highest probability mass at the upper bound, whereas the  
280 distribution of  $K_a$  in the SW model (Figure 2j) tends to become approximately normal. Overall, the marginal  
281 posterior probability density function of most of the individual parameters occupied only a relatively small  
282 region compared with the uniform prior distributions, and exhibited relatively large uncertainty reduction.

### 283 **3.2 Performance of the models**

284 The performance of each of the four ET models was evaluated over the course of the whole season in 2014.  
285 The calibrated parameters of the four models were used and individual ET models were run to estimate the  
286 half-hourly  $\lambda$ ET values. Table 3 summarizes the statistical results for the performance of the models using  
287 regression line slope,  $R^2$ , RMSE, MBE, IA, and EF. The regressions between measured and modeled  $\lambda$ ET values  
288 and MBE are shown in Figures 3 and 4, respectively.

289 In general, the four models produced slightly better fits to the measured  $\lambda$ ET for all the seasons with  $R^2$   
290 larger than 0.75 (Fig. 3). However, obvious discrepancies in the predictions made by the models were detected  
291 by comparing measured and modeled  $\lambda$ ET. According to the regression line slope and MBE, the PM model  
292 overestimated ET by 1% with a MBE of  $-9.52 \text{ W m}^{-2}$ , and the SW model overestimated ET by 5% with a  
293 relatively higher MBE of  $-19.07 \text{ W m}^{-2}$  compared to the PM model. The PT-FC and AA models tended to  
294 underestimate  $\lambda$ ET by 9% and 8% with an MBE of 25.42 and 23.29  $\text{W m}^{-2}$ , respectively. From a comparison  
295 between the slope and MBE, the PM model performance was higher than that of the other three models, with a  
296 slope almost equal to 1 and relatively lower MBE. The SW model was ranked second, while the performance of  
297 the AA model was slightly higher than that of the PT-FC model. However, if  $R^2$ , RMSE, IA, and EF were used  
298 to evaluate performance, the SW model had the best overall performance with  $R^2=0.83$ , RMSE= 76.34  $\text{W m}^{-2}$ ,  
299 IA = 0.95 and EF = 0.79. The second-best model was the PM model, and the PT-FC was ranked third, while the  
300 AA model ranked fourth. Based on the analysis of these traditional error metrics, the PT-FC and AA models  
301 yielded similar results. The observed and modeled  $\lambda$ ET for the four ET models were tightly grouped along the  
302 regression lines (Figure 3), and the PT-FC and AA models had similar modeled ET values with a similar degree  
303 of point scattering along the regression lines (Figure 3c-3d).

304 Figure 4 shows that large seasonal variations arise in MBE for the four ET models. From the variations in  
305 MBE, the estimated  $\lambda$ ET values for all models were generally lower than the measured values before the early

306 jointing stage of maize growth (DOY 154-177, left dashed line) and after the late maturity stage (DOY 256-265,  
307 right dash line) with the corresponding  $LAI < 2.5 \text{ m}^2 \text{ m}^{-2}$ . More positive MBE values for the PT-FC and AA  
308 models after the late maturity stage indicate their underestimated performances; however, these estimations  
309 appeared even more consistent with a symmetrical scattering of points along the 0-0 line (Figure 4c, 4d) during  
310 DOY 177-256 with  $LAI > 2.5 \text{ m}^2 \text{ m}^{-2}$ .

### 311 **3.3 Comparison of the models using BME**

312 Since there is currently no theoretical method for selecting power posterior  $\beta$  values, we determined these  
313 values using empirical but straightforward methods. For any power coefficient of  $\beta \in [0, 1]$ , a sample was drawn  
314 from the distribution  $p_\beta$  (Eq. 23) through running DREAM. Although adding more  $\beta_k$  values might improve the  
315 BME estimation, this was not done because of the computational cost. For each  $\beta_k$  value, at least 150,000  
316 DREAM simulations were large enough to ensure convergence. Figure 5 shows the evolution of  $\ln p(D|\theta, M)$   
317 for the four models as a function of  $\beta$  for a dataset covering the entire period. The BME for the SW model was  
318 substantially larger than that for the other three models, and the BME for the AA model was the smallest. The  
319 BME-based model ranking (from the best to the worst) is SW, PM, PT-FC, and AA. The PT-FC and AA models,  
320 which consist of the same number of parameters, had similar potential patterns of evolution with respect to the  
321 coefficient  $\beta_k$ . The results illustrate that with the addition of parameters, the model complexity and the model  
322 performance are both increased.

## 323 **4. Discussion**

### 324 **4.1 Parameter uncertainty analysis**

325 With regard to the efficiency of the DREAM algorithm, the acceptance rates of the PM (15.3%) and SW  
326 (18.9%) models were much higher than those obtained by some Markov Chain Monte Carlo (MCMC) algorithms  
327 that have been used in previous studies (Sadegh et al., 2014). The posterior parameter bounds exhibit a larger  
328 reduction using the DREAM algorithm compared with other studies using the Metropolis–Hasting algorithm.  
329 This demonstrates that DREAM could efficiently handle problems involving high-dimensionality, multimodality  
330 and nonlinearity.

331 The results showed that the assumed prior uncertainty ranges from most parameters in the four models

332 were significantly reduced. This indicates that the observed ET data contained sufficient information to estimate  
333 these parameters. Surface conductance  $g_s$  and modeled ET in the PM model are relatively insensitive to  $Q_{50}$ ,  $D_{50}$   
334 and  $K_q$ . Hence, these parameters could not be well constrained, and further relaxing the ranges for these  
335 parameters could not result in physically realistic behavior of the model. The calculation of  $g_s^c$  in the SW model  
336 is the same as in the PM model, and thus,  $g_s^c$  and modeled ET in the SW model are also insensitive to  
337 parameters of  $Q_{50}$ ,  $D_{50}$ ,  $K_q$ . Therefore, these three parameters were also not well constrained in the SW model. In  
338 addition, the uncertainties present in the edge-hitting parameters may be the outcome of model biases or  
339 EC-measured ET data errors, or the characteristic time scale of parameters governing the processes affecting ET  
340 is not exactly on the order of half-hours (Braswell et al., 2005). For example,  $Q_{50}$  and  $D_{50}$  govern changes in  
341 visible radiation flux and the humidity deficit at which stomatal conductance is half its maximum value,  
342 respectively, and these parameters may change over a shorter or longer time scale than half-hours.

343 The ecophysiological parameter  $g_{max}$  is a variable in the  $g_s^c$  equation in both the PM and SW models, but  
344 this parameter is sensitive to  $g_s^c$  and has a significant impact on the evaluated ET. Its effect is relatively  
345 independent compared to the other meteorological parameters in the models, and therefore this parameter was  
346 well specified in the PM and SW models. The posterior mean value of  $g_{max}$  ( $0.04 \text{ m s}^{-1}$ ) in the PM model from  
347 our study was close to that ( $0.05 \text{ m s}^{-1}$ ) reported in northwestern China (Li et al., 2013; Zhu et al., 2014), but  
348  $g_{max}$  ( $0.01 \text{ m s}^{-1}$ ) in the SW model was less than the reported value. Parameter  $\beta_l$  was well constrained in the  
349 PT-FC and AA models because it was relatively independent and did not directly relate to other observed  
350 variables.

351 Parameter  $K_a$  implicitly appears in the surface conductance equation (Eq.2) in PM model and  $K_a$  is  
352 insensitive to  $g_s$  and modeled ET (Leuning et al., 2008). In contrast,  $K_a$  is contained in the equation of net  
353 radiation flux into the substrate (Eq.10) in the SW model. This parameter can explicitly partition the total  
354 available energy into that absorbed by the canopy and by the soil in the SW model. An analysis of equation (10),  
355 found that the variation of  $K_a$  could not only account for the extinction effect but also correct the energy forcing  
356 data errors. This also meant that the estimated value of  $K_a$  using calibration data was actually not just the true  
357 extinction coefficient, but also included the energy imbalance correction in the SW model. From this analysis,  
358 we could see that  $K_a$  not only involved the distribution of energy between the canopy and the soil surface but

359 also the energy imbalance. Therefore, parameter  $K_a$  has a great influence on the performance of the SW model.  
360 This is why  $K_a$  is poorly constrained in the PM model but well constrained in the SW model. To further illustrate  
361 the insights regarding the influence of parameter  $K_a$  on the performance of the SW model, we calibrated the SW  
362 model again and reran the model with a constant value of  $K_a$ . The results showed a significant reduction in  
363 model performance when  $K_a$  was held constant. This implied that the main reason for the SW model  
364 outperforming the PM model in our study was not only the more physically rigorous structure of the SW model  
365 but also the key parameter  $K_a$  being well constrained in the SW model.

366 In general, parameters related to soil surface resistance in the SW model were well evaluated, while  
367 parameters related to canopy surface resistance in PM and SW models were poorly estimated. Therefore, using a  
368 reliable canopy surface resistance equation in the ET model was crucial for improving its performance. In  
369 addition, in our study, the traditional approach was used to quantify the uncertainty, which assumed that the  
370 uncertainty mainly arose because of the parameter uncertainty. However, this method cannot explicitly consider  
371 errors in the input data and model structural inadequacies. This is unrealistic for real applications, and it is  
372 desirable to develop a more reliable inference method to treat all sources of uncertainty separately and  
373 appropriately (Vrugt et al., 2008). Moreover, simultaneous direct measurement by micro-lysimeter of sap flow  
374 and daily soil evaporation will further help to constrain the model parameters.

#### 375 **4.2 Evaluation and selection of the models**

376 In this study, the traditional statistical measures and BME were chosen to evaluate and compare the  
377 performance of four ET models. From the respective composition of these measures, the statistical measures can  
378 be divided into residual-based metrics (such as regression slope and MBE) and squared-residual-based measures  
379 (such as  $R^2$ , RMSE, IA, and EF). The rankings of the models obtained using the same type of metric  
380 (residual-based or squared-residual-based) are similar. Slope and MBE, for example, which are both  
381 residual-based measures, produce identical rankings. However, the rankings produced by metrics of different  
382 types are not the same. For example, the PM model outperforms the SW model according to the residual-based  
383 metrics, but the performance of the PM model is worse than the SW model based on the squared-residual-based  
384 measures. The comparative analysis shows consistency between BME and the squared-residual-based metrics  
385 (hence the residual-based metrics disagreed with the BME measures). This reveals that the more complex SW  
386 model is the best model based on BME and squared-residual-based statistics. The rank order of overall



387 performance of the models from best to worst is SW, PM, PT-FC, and AA model.

388 Previous studies had shown that BME evaluated by TI provided estimates similar to the true values, and  
389 selected the true model if the true model was included within the candidate models (Marshall et al., 2005;  
390 Lartillot and Philippe, 2006). Meanwhile, some have argued that Bayesian analysis would choose the simplest  
391 model (Jefferys and Berger, 1992; Xie et al., 2011) because of the best trade-off between good fit with the data  
392 and model complexity (Schöniger et al., 2014). In this case, the most complex SW model had the highest BME  
393 and was chosen as the model with the best performance. This probably resulted from the fact that the complex  
394 SW model is indeed the most reliable model among the alternative ET models and can provide a good fit to  
395 justify its higher complexity. The SW model is a two-layer model, and simulates soil evaporation and plant  
396 transpiration separately, whereas the PM model is a single-layer model in which the plant transpiration and soil  
397 evaporation cannot be separated (Monteith, 1965). The PT-FC model is a simplified version of the PM model,  
398 and only requires meteorological and radiation information (Priestley and Taylor, 1972), whereas the AA model  
399 only relies on the feedback between actual ET and potential ET (Brutsaert and Stricker, 1979).

400 The results indicate that the squared-residual-based measures yielded the same rank order as the BME  
401 consistently, which makes the squared-residual-based metrics seemed to identify a reasonable rank order.  
402 However, this has not been the general case, since the error metrics and BME belong to different types of model  
403 selection and there are differences in the behavior and optimality of the two types of model selection. BME is a  
404 consistent model selection which tries to identify which of the models produced the observed data. Conversely,  
405 nonconsistent model selection uses the available data to estimate which of the models might be best in  
406 predicting future data. In fact, the error metrics are essentially nonparsimonious model selection, which is a  
407 special case of nonconsistent model selection. The simple traditional statistical measures were known to usually  
408 provide a biased view of the efficacy of a model (Kessler and Neas, 1994; Legates and McCabe, 1999), where  
409 only the goodness of fit is used for rating models without penalizing the model complexity and thus lacking  
410 consistency for the selected model (Höge et al., 2018). In addition, sensitivity to outliers is associated with these  
411 metrics and leads to relatively high values due to the squaring of the residual terms (Willmott, 1981).  
412 Furthermore, these traditional statistical metrics ignore the priors, which is in fact used in Bayesian analysis.  
413 PT-FC and AA, provide identical estimates of  $R^2$  and IA. This is most likely because both models had the same  
414 dimension and a similar model structure. Marshall et al. (2005) argued that EF would provide an incorrect

415 conclusion, and Samani et al. (2018) suggested that RMSE would select the complex model as the best  
416 performing model. As for the slope and MBE, the rankings produced by these residual-based metrics were in  
417 obvious disagreement with the one based on BME. Part of the lower simulation values could be  
418 counter-balanced by the higher values of that in the slope and MBE methods, thus these criteria provide an  
419 erroneous and unreliable evaluation of the models. Therefore, the squared-residual-based and residual-based  
420 measures were not certain to provide reasonable results in terms of model ranking. The consistency between  
421 BME and the squared-residual-based metrics only indicates that the optimal model evaluated by BME would  
422 also provide the best predictions, and thus consistent model selection should also be asymptotically efficient  
423 (Leeb & P ätscher, 2009; Shao, 1997).

#### 424 **4.3 Analysis of model-data mismatch**

425 Conceptual and structural inadequacies of the hydrological model together with measurement errors of the  
426 model input (forcing) and output (calibration) data introduce errors in the estimated parameters and model  
427 simulations (Laloy, 2015). Hydrological systems are indeed heavily input-driven and errors in forcing data can  
428 dramatically impair the quality of calibration results and model output (Bardossy and Das, 2008; Giudice, 2015).  
429 Measurement errors occur for a variety of reasons, including unreasonable gap-filling in rainy days; dew and fog;  
430 inadequate areal coverage of point-scale soil water measurement; mechanical limitations of the EC system; and  
431 inaccurate measurements of wind-speed, soil water, radiation and vapor pressure deficit. ET process is described  
432 using equations that can only capture parts of the complex natural processes and any ET model is an inherent  
433 simplification of the real system. These inadequacies can thus lead to biased parameters and implausible  
434 predictions.

435 In our study, the results indicated that the PM and SW models overestimated the half-hourly ET compared  
436 to the measured ET. Several studies also indicated that ET was overestimated by the PM model (Fisher et al.,  
437 2005; Ortega-Farias et al., 2006; Li et al., 2015) and the SW model (Li et al., 2013; Li et al., 2015; Zhang et al.,  
438 2008). Possible reasons for the inaccurate estimates included the following: (1) Anisotropic turbulence with  
439 weak vertical and strong horizontal fluctuation leads to energy imbalance. The total turbulent heat flux was  
440 lower by ~10–30% compared to the available energy in many land surface experiments (Tsvang et al., 1991;  
441 Beyrich et al., 2002; Oncley et al., 2007; Foken et al., 2010) and influx networks (Franssen et al., 2010). Liang  
442 et al. (2017) also showed an energy imbalance result in the semiarid area in China, and indicated that the energy

443 balance closure ratio ranged from 0.52 to 0.90 during the day, whereas it was about 0.25 at night. However, the  
444 measured ET only included vertical flux and not horizontal flux, leading to the measured ET being lower than  
445 that of ET predicted by the PM and SW models using the available energy. (2) The absence of a mechanistic  
446 representation of the physiological response to plant hydrodynamics makes it difficult for the available ET  
447 models to resolve the dynamics of intradaily hysteresis, producing patterns of diurnal error, while the imbalance  
448 or lack of between-leaf water demand and soil water supply imposes hydrodynamic limitations on stomatal  
449 conductance (Thomsen et al., 2013; Zhang et al., 2014; Matheny et al., 2014). Li et al. (2015) also concluded  
450 that neglecting the restrictive effect of the soil on water transport in empirical canopy resistance equations can  
451 result in large errors in the partial canopy stage. However, these equations can estimate ET accurately under the  
452 full canopy stage (Alves and Pereira, 2000; Katerji and Rana, 2006; Katerji et al., 2011; Rana et al., 2011). Li et  
453 al. (2015) showed that the PM model combined with canopy resistance overestimated maize ET during the  
454 partial and dense canopy stages by 16% and 13%, respectively. Moreover, in a study of ET in vineyards,  
455 Leuning (2008) found that the PM model coupled with canopy resistance overestimated ET during the entire  
456 growth stage by 29%.

457 The estimates for ET produced by the PT-FC and AA models were generally lower than the measured  
458 values during the entire season. In addition, the four models also underestimated ET during periods of partial  
459 cover ( $LAI < 2.5 \text{ m}^2 \text{ m}^{-2}$ ). The PT-FC and AA models consistently underestimated ET, especially during the late  
460 maturity stage. The underestimation probably resulted from the following: (1) Non classical situations, such as  
461 the oasis effect, may occur in the study area. Strong evaporation from the moist ground and plants results in  
462 latent heat cooling. However, this upward latent heat flux was opposed by a downward sensible heat flux from  
463 the warm air to the cool ground, and thus the latent heat flux was positive while the sensible heat flux is  
464 negative. Therefore, the latent heat flux can be greater in magnitude than the solar heating, because of the  
465 additional energy extracted from the warm air by evaporation (Stull, 1988). (2) The lack of mechanistic  
466 representation of rainfall interception in ET models probably led to inaccurate simulation for periods soon after  
467 rainy days. Bohn and Vivoni (2016) found that evaporation of canopy interception accounted for 8% of the  
468 annual ET across the North American monsoon region. Comparing the AA and PT-FC models, the former  
469 includes forcing data of available radiation, soil water content and relative humidity, but the PT-FC model only  
470 requires available radiation and soil water content and is independent of relative humidity. However, the similar  
471 statistical results and similar degrees of MBE scatter indicate that relative humidity has little influence on the

472 AA model simulation. The consistent and consecutive underestimation of ET by the PT-FC and AA models  
473 during the late maturity stage show that the model-data disagreement is not caused by regional advection and  
474 rainfall interception, because atmospheric processes and thermally-induced circulation can only occur at certain  
475 times and during certain days. Therefore, we think that the consistent underestimation of ET by the PT-FC and  
476 AA models results primarily from conceptual and structural inadequacies, energy imbalance, and soil water  
477 stress. Although the PM and SW models share a common theoretical basis and the PT-FC model is a  
478 simplification of the PM model, these models perform significantly differently. Part of the overestimation of ET  
479 by the PM and SW models, caused by coupling with the canopy resistance, may be offset by underestimation  
480 caused by energy imbalance and soil water stress. However, underestimation of ET by the PT-FC and AA  
481 models cannot be counterbalanced by overestimation during the later maturity stage because the PT-FC and AA  
482 models are independent of the canopy resistance. Consequently, the half-hourly patterns of errors in the  
483 estimates of ET by the PM and SW models are characterized by symmetry and a low degree of scatter, but the  
484 PT-FC and AA models exhibit consistently asymmetrical error patterns. By contrast, other studies showed that  
485 the PM model (Kato et al., 2004) and the SW model (Chen et al., 2015) underestimated half-hourly ET. As for  
486 the PT-FC and AA models, some studies reported that the PT-JPL (Zhang et al., 2017) and the AA model showed  
487 an overall poor performance (Zhang et al., 2017). While other studies have indicated that the AA method  
488 performed well for both maize and canola crops (Liu et al., 2012). Therefore, the performance of the four ET  
489 models appears to vary not only for different crops and locations but also for different meteorological,  
490 physiological and soil conditions. Moreover, the performance is also related to the stage of crop growth. Note  
491 that these conclusions about the ET models evaluation are derived from traditional error metrics rather than  
492 those based on BME model selection. It would be desirable to use available data from other study areas or from  
493 other crops for BME-based model selection to confirm whether the SW model is the optimal model under other  
494 conditions. Overall, combined with the parameter uncertainty analysis described in Section 4.1, we conclude that  
495 energy imbalance and energy interaction between canopy and soil surface have a greater impact on the model  
496 performance. And thus, explicitly treating of energy error, and incorporating the elements of existing hydrologic  
497 theory about energy interaction between canopy and surface or conceptually correcting the energy interaction  
498 are a practicable option for model improvement and application.

## 499 **5. Conclusions**

500 This study illustrated the application of the Bayesian approach on the statistical analysis and model

501 selection of four widely used ET models. The results showed that the DREAM algorithm successfully reduced  
502 the assumed prior uncertainties for most of the parameters in the four models. In the model calibration, the key  
503 parameters which had a significant influence on ET simulations were well constrained. The main reasons for the  
504 outperforming of SW model were its physically rigorous structure and the extinction coefficient parameter,  
505 which is sensitive and has a significant impact on the performance of the model, being well constrained. BME is  
506 a consistent model selection to identify the best fitting to the observed data. Although the squared-residual-based  
507 metrics, including  $R^2$ , IA, RMSE, and EF, produced a ranking identical to that of BME, it must be noted that  
508 these squared-residual-based metrics do not allow using prior information and do not penalize the model  
509 complexity when comparing the models. Therefore, some cautions are needed when using these statistical  
510 methods to compare different models.

511 The model–data discrepancies were analyzed to facilitate model improvement after Bayesian model  
512 calibration and comparison. The results indicate that the discrepancies arose mainly as a result of energy  
513 imbalance caused by anisotropic turbulence, additional energy induced by advection processes, the absence of a  
514 mechanistic representation of the physiological response to plant hydrodynamics and the energy interaction  
515 between canopy and surface. Among these causes, energy imbalance and additional energy are related to forcing  
516 data errors rather than to an unreasonable model structure. Thus, understanding the process of the physiological  
517 response to plant hydrodynamics and the interaction between canopy and surface is essential for improving the  
518 performance of evapotranspiration models. Overall, the applications of Bayesian calibration, Bayesian model  
519 evaluation and analysis of model–data discrepancies in our study, provide a promising framework for reducing  
520 uncertainty and improving the performance of ET models. It would be desirable to confirm whether the SW is  
521 the optimal model using data of other crops or other climate regions.

## 522 **Author contribution**

523 Guoxiao Wei and Xiaoying Zhang designed the experiments. Ning Yue and Fei Kan carried them out.  
524 Ming Ye developed the model selection scheme. Guoxiao Wei performed the simulations. Guoxiao Wei and  
525 Xiaoying Zhang prepared the manuscript with contributions from all co-authors.

## 526 **Competing interests**

527 The authors declare that they have no conflict of interest.

## 528 Acknowledgments

529 We thank Ying Guo, Huihui Dang, Jun Dong for the data collection and analysis. This work was funded by  
530 the National Natural Science Foundation of China Nos. 41471023 and Nos.41702244. The third author was  
531 supported in part by DOE Early Career Award DE-SC0008272 and National Science Foundation-Division of  
532 Earth Science Grant 1552329. All observed data used in this study are from Heihe Watershed Allied Telemetry  
533 Experimental Research (HiWATER). We thank all the staff who participated in HiWATER field campaigns.  
534 Considerate and helpful comments by anonymous reviewers have considerably improved the manuscript.

## 535 References

- 536 Allen, R. G., Perista, L. S., Raes, D., and Smith, M.: Crop Evapotranspiration-Guidelines for Computing Crop  
537 Water Requirements; FAO Irrigation and Drainage apers-56, FAO-Food and Agriculture Organization  
538 of the United Nations, Rome, 1998.
- 539 Alves, I. and Pereira, L. S.: Modeling surface resistance from climatic variables? *Agric. Water Manage.*, 42,  
540 371–385, 2000.
- 541 Aubinet, M., Grelle, A., Ibrom, A., Rannik, Ü., Moncrieff, J., and Foken, T.: Estimates of the annual net carbon  
542 and water exchange of forests: the euroflux methodology, *Adv. Ecol. Res.*, 30(1), 113-175, 2000.
- 543 Baldocchi, D. D.: Assessing the eddy covariance technique for evaluating carbon dioxide exchange rates of  
544 ecosystems: past, present and future, *Glob. Change. Biol.*, 9, 479–492, 2003.
- 545 Bardossy, A., and Das, T.: Influence of rainfall observation network on model calibration and application,  
546 *Hydrol. Earth Syst. Sci.*, 12(1), 77-89, doi:10.5194/hess-12-77-2008, 2008.
- 547 Barton, I. J.: A Parameterization of the Evaporation from Nonsaturated Surfaces, *J. Appl Meteorol.*, 18(1), 43-47,  
548 1979.
- 549 Beyrich, F., Richter, S. H., Weisensee, U., Kohsiek, W., Lohse, H., de Bruin, H. A. R., Foken, T., Göckede, M.,  
550 Berger, F., Vogt, R., and Batchvarova, E.: Experimental determination of turbulent fluxes over the  
551 heterogeneous litfass area: selected results from the litfass-98 experiment, *Theor. Appl. Climatol.*,  
552 73(1–2), 19–34, doi:10.1007/s00704-002-0691-7, 2002.
- 553 Bohn, T. J., and Vivoni, E. R.: Process-based characterization of evapotranspiration sources over the North  
554 American monsoon region, *Water Resour. Res.*, 52, 358–384, doi:10.1002/2015WR017934, 2016.
- 555 Bonan, G.: *Ecological climatology: concepts and applications*, Cambridge University Press, 2008.
- 556 Braswell, B. H., Sacks, W. J., Linder, E., and Schimel, D. S.: Estimating diurnal to annual ecosystem parameters  
557 by synthesis of a carbon flux model with eddy covariance net ecosystem exchange observations, *Global.*  
558 *Change. Biol.*, 11, 335–355, 2005,
- 559 Brutsaert, W., and Han, S.: An advection-aridity approach to estimate actual regional evapotranspiration, *Water*  
560 *Resour. Res.*, 15(2), 443-450, 1979.
- 561 Brutsaert, W.: *Hydrology: An Introduction*. Cambridge University Press, Cambridge, 2005.
- 562 Chen, D. Y., Wang, X., Liu, S. Y., Wang, Y. K., Gao, Z. Y., Zhang, L. L., Wei, X. G., and Wei, X. D.: Using  
563 Bayesian analysis to compare the performance of three evapotranspiration models for rainfed jujube  
564 (*Ziziphus jujuba* Mill.) plantations in the Loess Plateau, *Agr. Water. Manage.*, 159, 341–357, 2015.
- 565 Elshall, A. S., Ye, M., Pei, Y., Zhang, F., Niu, G. Y., and Barron-Gafford, G. A.: Relative model score: A scoring  
566 rule for evaluating ensemble simulations with application to microbial soil respiration modeling, *Stoch.*  
567 *Env. Res. A.*, 1-11, DOI: 10.1007/s00477-018-1592-3, 2018.
- 568 Ershadi, A., McCabe, M. F., Evans, J. P., Chaney, N. W., and Wood, E. F.: Multi-site evaluation of terrestrial  
569 evaporation models using fluxnet data, *Agric. For. Meteorol.*, 187(8), 46-61, 2014.
- 570 Ershadi, A., McCabe, M. F., Evans, J. P., and Wood, E. F.: Impact of model structure and parameterization on  
571 Penman–Monteith type evaporation models, *J. Hydrol.*, 525, 521–535, 2015.
- 572 Fisher, J. B., DeBiase, T. A., Qi, Y., Xu, M., and Goldstein, A. H.: Evapotranspiration models compared on a  
573 Sierra Nevada forest ecosystem, *Environ. Model. Softw.*, 20 (6), 783–796, 2005.

- 574 Flint A. L., Childs, S. W.: Use of the Priestley–Taylor evaporation equation for soil water limited conditions in a  
575 small forest clearcut, *Agric. For. Meteorol.*, 56(3–4), 247–260, 1991.
- 576 Foken, T., Mauder, M., Liebethal, C., Wimmer, F., Beyrich, F., Leps, J. P., Raasch, S., DeBruin, H. A. R.,  
577 Meijninger, W. M. L., and Bange, J.: Energy balance closure for the LITFASS-2003 experiment, *Theor.*  
578 *Appl. Climatol.*, 101(1–2), 149–160, doi:10.1007/s00704-009-0216-8, 2010.
- 579 Franssen, H. J. H., Stöckli, R., Lehner, I., Rotenberg, E., and Seneviratne S. I.: Energy balance closure of  
580 eddy-covariance data: A multisite analysis for European FLUXNET stations, *Agric. For. Meteorol.*,  
581 150(12), 1553–1567, doi:10.1016/j.agrformet.2010.08.005, 2010.
- 582 Gelman, A., and Rubin, D. B.: Inference from iterative simulation using multiple sequences, *Stat. Sci.*, 7, 457–  
583 472, 1992.
- 584 Gelman, A.: Simulating normalizing constants: From importance sampling to bridge sampling to path sampling,  
585 *Stat. Sci.* 13, 163–185, 1998.
- 586 Giudice, D., Albert, C., Rieckermann, J., and Reichert, P.: Describing the catchment-averaged precipitation as a  
587 stochastic process improves parameter and input estimation, *Water Resour. Res.*, 52, 3162–3186,  
588 doi:10.1002/2015WR017871, 2016.
- 589 Höge, M., Wähling, T., and Nowak, W.: A primer for model selection: The decisive role of model complexity.  
590 *Water Resour. Res.*, 54, 1688–1715, doi.org/10.1002/2017WR021902, 2018.
- 591 Jefferys, W. H., and Berger, J. O.: Sharpening Ockham’s razor on a Bayesian strop, *Am. Sci.*, 89, 64–72, 1992.
- 592 Kashyap, R. L.: Optimal choice of AR and MA parts in autoregressive moving average models, *IEEE Trans.*  
593 *Pattern Anal. Mach. Intell.*, 4(2), 99–104, 1982.
- 594 Katerji, N., and Rana, G.: Modelling evapotranspiration of six irrigated crops under Mediterranean climate  
595 conditions, *Agric. For. Meteorol.*, 138, 142–155, 2006.
- 596 Katerji, N., Rana, G., Fahed, S.: Parameterizing canopy resistance using mechanistic and semi-empirical  
597 estimates of hourly evapotranspiration: critical evaluation for irrigated crops in the Mediterranean,  
598 *Hydrol. Process.*, 25, 117–129, 2011.
- 599 Kato, T., Kimura, R., and Kamichika, M.: Estimation of evapotranspiration, transpiration ratio and water-use  
600 efficiency from a sparse canopy using a compartment model, *Agric. Water Manage.*, 65, 173–191,  
601 2004.
- 602 Kessler, E., and Neas, B.: On correlation, with applications to the radar and raingage measurement of rainfall,  
603 *Atmos. Res.*, 34, 217–229, 1994.
- 604 Laloy, E., Linde, N., Jacques, D., and Vrugt, J. A.: Probabilistic inference of multi-Gaussian fields from indirect  
605 hydrological data using circulant embedding and dimensionality reduction, *Water Resour. Res.*, 51,  
606 4224–4243, doi:10.1002/2014WR016395, 2015.
- 607 Lartillot, N., and Philippe, H.: Computing Bayes factors using thermodynamic integration, *Syst. Biol.*, 55(2),  
608 195–207, 2006.
- 609 Leeb, H., and Pötscher, B. M.: Model selection, Berlin, Germany: Springer., pp, 889–925,  
610 doi.org/10.1007/978-3-540-71297-839, 2009.
- 611 Legates, D. R., and McCabe, G. J.: Evaluating the use of “goodness-of-fit” measures in hydrologic and  
612 hydroclimatic model validation, *Water Resour. Res.*, 35, 233–241, 1999.
- 613 Leuning, R., Zhang, Y. Q., Rajaud, A., Cleugh, H., and Tu, K.: A simple surface conductance model to estimate  
614 regional evaporation using MODIS leaf area index and the Penman–Monteith equation, *Water Resour.*  
615 *Res.*, 44, W10419, doi.org/10.1029/2007WR006562, 2008.
- 616 Liang, J., Zhang, L., Cao, X., Wen, J., Wang, J., and Wang, G.: Energy balance in the semiarid area of the Loess  
617 Plateau, China, *J. Geophys. Res. Atmos.*, 122, 2155–2168, doi:10.1002/2015JD024572, 2017.
- 618 Li, S., Kang, S., Zhang, L., Ortega-Farias, S., Li, F., Du, T., Tong, L., Wang, S., Ingman, M., and Guo, W.:  
619 Measuring and modeling maize evapotranspiration under plastic film-mulching condition, *J. Hydrol.*,  
620 503, 153–168, 2013.
- 621 Li, S., Zhang, L., Kang, S., Tong, L., Du, T., Hao, X., Zhao, P.: Comparison of several surface resistance models  
622 for estimating crop evapotranspiration over the entire growing season in arid regions. *Agric. For.*  
623 *Meteorol.* 208, 1–15, 2015.
- 624 Li, X., Cheng, G. D., Liu, S. M., Xiao, Q., Ma, M. G., Jin, R., Che, T., Liu, Q. H., Wang, W. Z., Qi, Y., Wen, J.  
625 G., Li, H. Y., Zhu, G. F., Guo, J. W., Ran, Y. H., Wang, S. G., Zhu, Z. L., Zhou, J., Hu, X. L., and Xu, Z.  
626 W.: Heihe Watershed Allied Telemetry Experimental Research (HiWATER): Scientific objectives and  
627 experimental design, *B. Am. Meteorol. Soc.*, 94, 1145–1160, 2013.
- 628 Liu, S. M., Xu, Z. W., Wang, W. Z., Jia, Z. Z., Zhu, M. J., Bai, J., and Wang, J. M.: A comparison of

629 eddy-covariance and large aperture scintillometer measurements with respect to the energy  
630 balance closure problem, *Hydrol. Earth Syst. Sci.*, 15, 1291–1306, doi:10.5194/hess-15-1291-2011,  
631 2011.

632 Liu, G., Liu, Y., Hafeez, M., Xu, D., Vote, C.: Comparison of two methods to derive time series of actual  
633 evapotranspiration using eddy covariance measurements in the southeastern Australia, *J. Hydrol.*,  
634 454–455 (4), 1–6, 2012.

635 Liu, P., Elshall, A. S., Ye, M., Beerli, P., Zeng, X., Lu, D., and Tao, Y.: Evaluating marginal likelihood with  
636 thermodynamic integration method and comparison with several other numerical methods. *Water*  
637 *Resour. Res.*, 52(2), 734-758, doi:10.1002/2014WR016718, 2016.

638 Marshall, L., Nott, D., and Sharma, A.: Hydrological model selection: A Bayesian alternative, *Water Resour.*  
639 *Res.*, 41(10), 3092-3100, doi: 10.1029/2004WR003719, 2005.

640 Matheny, A. M., Bohrer, G., Stoy, P. C., Baker, I. T., Black, A. T., Desai, A. R., Dietze, M. C., Gough, C. M.,  
641 Ivanov, V. Y., Jassal, R. S., Novick, K. A., Schäfer, K. V. R., and Verbeeck, H.: Characterizing the  
642 diurnal patterns of errors in the prediction of evapotranspiration by several land-surface models: An  
643 NACP analysis, *J. Geophys. Res. Biogeosci.*, 119(7), 1458-1473, 2014.

644 Monteith, J. L.: Evaporation and environment, *Symp. Soc. Exp. Biol.*, 19, 205–234, 1965.

645 Morison, J. I. L., Baker, N. R., Mullineaux, P. M., and Davies, W. J.: Improving water use in crop production,  
646 *Philos. T. Roy. Soc. B.*, 363, 639–658, 2008.

647 Neal, R. M.: Markov chain sampling methods for Dirichlet process mixture models, *J. Comput. Graph. Stat.*, 9,  
648 249–265, 2000.

649 Oncley, S. P., Foken, T., Vogt, R., Kohsiek, W., DeBruin, H., Bernhofer, C., Christen, A., Van Gorsel, E., Grantz,  
650 D., and Feigenwinter, C.: The energy balance experiment EBEX-2000. Part I: Overview and energy  
651 balance, *Boundary Layer Meteorol.*, 123(1), 1–28, doi:10.1007/s10546-007-9161-1, 2007.

652 Ortega-Farias, S., Olioso, A., Fuentes, S., and Valdes, H.: Latent heat flux over a furrow-irrigated tomato crop  
653 using Penman–Monteith equation with a variable surface canopy resistance, *Agric. Water Manage.*, 82,  
654 421–432, 2006.

655 Ortega-Farias, S., Poblote-Echeverria, C., and Brisson, N.: Parameterization of a two-layer model for estimating  
656 vineyard evapotranspiration using meteorological measurements, *Agr. For. Meteorol.*, 150, 276–286,  
657 2010.

658 Parlange, M. B., and Katul, G. G.: An advection-aridity evaporation model, *Water Resour. Res.*, 28 (1), 127-132,  
659 1992.

660 Poblote-Echeverria, C., and Ortega-Farias, S.: Estimation of actual evapotranspiration for a drip-irrigated Merlot  
661 vineyard using a three-source model, *Irrig. Sci.*, 28, 65–78, 2009.

662 Priestley, C. H. B., and Taylor, R. J.: On the assessment of surface heat flux and evaporation using large-scale  
663 parameters, *Mon. Weather Rev.*, 100 (2), 81-92, 1972.

664 Rana, G., Katerji, N., Ferrara, R.M., and Martinelli, N.: An operational model to estimate hourly and daily crop  
665 evapotranspiration in hilly terrain: validation on wheat and oat crops, *Theory Appl. Climatol.*, 103,  
666 413–426, 2011.

667 Sadegh, M., and Vrugt J. A.: Approximate Bayesian Computation using Markov Chain Monte Carlo simulation:  
668 DREAM(ABC), *Water Resour. Res.*, 50, 6767–6787, doi:10.1002/2014WR015386, 2014.

669 Samani, S., Ye, M., Zhang, F., Pei, Y. Z., Tang, G. P., Elshall, A. S., and Moghaddam, A. A.: Impacts of prior  
670 parameter distributions on bayesian evaluation of groundwater model complexity, *Water Science &*  
671 *Engineering.*, 11(2), 89-100, doi.org/10.1016/j.wse.2018.06.001, 2018.

672 Schöniger, A., Wohling, T., Samaniego, L., and Nowak, W.: Model selection on solid ground: Rigorous  
673 comparison of nine ways to evaluate Bayesian model evidence, *Water Resour. Res.*, 50, 9484–9513,  
674 doi:10.1002/2014WR016062, 2014.

675 Schwarz, G.: Estimating the dimension of a model, *Ann. Stat.*, 6(2), 461–464, doi:10.1214/aos/1176344136,  
676 1978.

677 Shao, J.: An asymptotic theory for linear model selection, *Statistica Sinica*, 7(2), 221–242, 1997.

678 Shuttleworth, W. J., Gurney, R. J.: The theoretical relationship between foliage temperature and canopy  
679 resistance in sparse crops, *Q. J. Roy. Meteorol. Soc.*, 116, 497–519, 1990.

680 Stannard, D. I.: Comparison of Penman-Monteith, Shuttleworth-Wallace, and modified Priestley-Taylor  
681 evapotranspiration models for wildland vegetation in semiarid rangeland, *Water Resour. Res.*, 29 (5),  
682 1379-1392, 1993.

683 Stull, R. B.: An introduction to boundary layer meteorology, Kluwer Academic Publ., 255pp, 1988.



- 684 Sumner, D. M., and Jacobs, J. M.: Utility of Penman–Monteith Priestley–Taylor reference evapotranspiration,  
685 and pan evaporation methods to estimate pasture evapotranspiration, *J. Hydrol.*, 308 (1-4), 81-104,  
686 2005.
- 687 Szilagyi, J., and Jozsa, J.: New findings about the complementary relationship based evaporation estimation  
688 methods, *J. Hydrol.*, 354: 171–186, 2008.
- 689 Thomsen, J., Bohrer, G., Matheny, M. V., Ivanov, Y., He, L., Renninger, H., and Schäfer, K.: Contrasting  
690 hydraulic strategies during dry soil conditions in *Quercus rubra* and *Acer rubrum* in a sandy site in  
691 Michigan, *Forests.*, 4(4), 1106–1120, 2013.
- 692 Tsvang, L., Fedorov, M., Kader, B., Zubkovskii, S., Foken, T., Richter, S., and Zeleny, Y.: Turbulent exchange  
693 over a surface with chessboardtype inhomogeneities, *Boundary Layer Meteorol.*, 55(1–2), 141–160,  
694 1991.
- 695 Vinukollu R, K., Wood, E. F., Ferguson, C. R., and Fisher, J. B.: Global estimates of evapotranspiration for  
696 climate studies using multi-sensor remote sensing data: evaluation of three process-based approaches,  
697 *Remote Sens. Environ.*, 115(3), 801–823, 2011.
- 698 Vrugt, J. A., ter Braak, C. J. F., Clark, M. P. J., Hyman, M., and Robinson, B. A.: Treatment of input uncertainty  
699 in hydrologic modeling: Doing hydrology backward with Markov chain Monte Carlo simulation, *Water  
700 Resour. Res.*, 44, W00B09, doi:10.1029/2007WR006720, 2008.
- 701 Vrugt, J. A., ter Braak, C. J. F., Diks, C. G. H., Higdon, D., Robinson, B. A., and Hyman, J. M.: Accelerating  
702 Markov chain Monte Carlo simulation by differential evolution with self-adaptive randomized  
703 subspace sampling, *Int. J. Nonlinear Sci. Numer. Simul.*, 10(3), 273-290, 2009.
- 704 Webb, E. K., Pearman, G. I., and Leuning, R.: Correction of flux measurements for density effects due to heat  
705 and water-vapor transfer, *Q. J. R. Meteorol. Soc.*, 106(447), 85–100, 1980.
- 706 Willmott, C. J.: On the validation of models, *Phys. Geogr.*, 2, 184-194, 1981.
- 707 Xie, W., Lewis, P. O., Fan, Y., Kuo, L., and Chen, M. H.: Improving marginal likelihood estimator for Bayesian  
708 phylogenetic model selection, *Syst. Biol.*, 60(2), 150-160, 2011.
- 709 Xu, C. Y., and Singh, V. P.: A review on monthly water balance models for water resources investigations, *Water  
710 Resour. Manage.*, 12, 31-50, 1998.
- 711 Xu, Z. W., Liu, S. M., Li, X., Shi, S. J., Wang, J. M., Zhu, Z. L., Xu, T. R., Wang, W. Z., and Ma, M. G.:  
712 Intercomparison of surface energy flux measurement systems used during the HiWATERUSOEXE, *J.  
713 Geophys. Res.*, 118, 13140–13157, 2014.
- 714 Ye, M., Neuman, S. P., and Meyer, P. D.: Maximum likelihood Bayesian averaging of spatial variability models  
715 in unsaturated fractured tuff, *Water Resour. Res.*, 40, W05113, doi:10.1029/2003WR002557, 2004.
- 716 Ye, M., Meyer, P. D., and Neuman, S. P.: On model selection criteria in multimodel analysis, *Water Resour. Res.*,  
717 44, W03428, doi:10.1029/2008WR006803, 2008.
- 718 Zhang, B., Kang, S., Li, F., and Zhang, L.: Comparison of three evapotranspiration models to Bowen  
719 ratio-energy balance method for vineyard in an arid desert region of northwest China, *Agr. Forest  
720 Meteorol.*, 148: 1629–1640, 2008.
- 721 Zhang, X. Y., Liu, C. X., Hu, B. X., and Zhang, G. N.: Uncertainty analysis of multi-rate kinetics of uranium  
722 desorption from sediments, *J. Contam. Hydrol.*, 156(1), 1-15, 2014.
- 723 Zhang, K., Ma, J., Zhu, G., Ma, T., Han, T., and Feng, L. L.: Parameter sensitivity analysis and optimization for  
724 a satellite-based evapotranspiration model across multiple sites using moderate resolution imaging  
725 spectroradiometer and flux data. *Journal of Geophysical Research: Atmospheres*, 122(1), 230-245,  
726 2017.
- 727 Zhu, G. F., Su, Y. H., Li, X., Zhang, K., and Li, C. B.: Estimating actual evapotranspiration from an alpine  
728 grassland on Qinghai–Tibetan plateau using a two-source model and parameter uncertainty analysis by  
729 Bayesian approach, *J. Hydrol.*, 476, 42–51, 2013.
- 730 Zhu, G. F., Li, X., Su, Y. H., Zhang, K., Bai, Y., Ma, J. Z., Li, C. B., Hu, X. L., and He, J. H.: Simultaneously  
731 assimilating multivariate data sets into the two-source evapotranspiration model by Bayesian approach:  
732 Application to spring maize in an arid region of northwestern China, *Geosci. Model. Dev.*, 7(4),  
733 1467–1482, 2014.

#### 734 **Appendix A: List of symbols and physical characteristics in ET models**

A	Available energy for the whole canopy ( $Wm^{-2}$ )
$A_s$	Available energy for the soil surface ( $W m^{-2}$ )

$R_n$	Net radiation fluxes into the canopy ( $\text{W m}^{-2}$ )
$R_{ns}$	Net radiation flux into the substrate ( $\text{W m}^{-2}$ )
$G$	Soil heat flux ( $\text{W m}^{-2}$ )
$\lambda ET$	Sum of the latent heat flux from the crop ( $\lambda T$ ) and soil ( $\lambda E$ ) ( $\text{W m}^{-2}$ )
$ET_c$	Canopy transpiration ( $\text{W m}^{-2}$ )
$ET_s$	Soil evaporation ( $\text{W m}^{-2}$ )
$C_c$	Canopy resistance coefficient (dimensionless)
$C_s$	Soil surface resistance coefficient (dimensionless)
$LAI$	Leaf area index
$Q_{50}$	Visible radiation flux when stomatal conductance is half its maximum value ( $\text{W m}^{-2}$ )
$D_{50}$	Vapor pressure deficit at which stomatal conductance is half its maximum value (kPa)
$D_a$	Vapor pressure deficit at the reference height ( $D_a = e_s - e_a$ ) (kPa)
$Q_h$	Flux density of visible radiation at the top of the canopy ( $\text{W m}^{-2}$ )
$K_q$	Extinction coefficient
$K_a$	Extinction coefficient
$f$	Fraction of evaporation soil and total evaporation
$\lambda$	Latent heat of water evaporation ( $\text{MJ kg}^{-1}$ )
$\Delta$	Slope of the saturated vapour pressure curve ( $\text{Pa K}^{-1}$ )
$\gamma$	Psychrometric constant ( $\text{kPa K}^{-1}$ )
$\rho$	Density of air ( $\text{kg m}^{-3}$ )
$k$	Karman constant (0.41)
$e_s$	Saturated vapor pressure (kPa)
$e_a$	Actual vapor pressure (kPa)
$q^*$	Saturation-specific humidity at air temperature ( $\text{kg kg}^{-1}$ )
$q$	Specific humidity of the atmosphere ( $\text{kg kg}^{-1}$ )
$b_1$	Empirical constant ( $\text{s m}^{-1}$ )
$b_2$	Empirical constant ( $\text{s m}^{-1}$ )
$\beta_1$	empirical constant
$\beta_2$	empirical constant
$\theta$	Soil water content ( $\text{m}^3 \text{m}^{-3}$ )
$\theta_a$	Critical water content at which plant stress starts ( $\text{m}^3 \text{m}^{-3}$ )
$\theta_b$	Water content at the wilting point ( $\text{m}^3 \text{m}^{-3}$ )
$\theta_r$	Residual soil water content ( $\text{m}^3 \text{m}^{-3}$ )
$\theta_s$	Saturated water content ( $\text{m}^3 \text{m}^{-3}$ )
$\Theta$	Relative water saturation
$d$	Zero plane displacement height (m)
$z_m$	Height of the wind speed and humidity measurements (3 m)
$z_{0m}$	Roughness length governing the transfer of momentum (m)
$z_{0v}$	Roughness length governing the transfer of water vapor (m)
$h$	Canopy height (m)
$u_z$	Wind speed at height $z_m$ ( $\text{m s}^{-1}$ )
$g_a$	Aerodynamic conductance ( $\text{m s}^{-1}$ )
$g_s$	Surface conductance ( $\text{m s}^{-1}$ )
$g_{max}$	Maximum stomatal conductance of leaves at the top of the canopy ( $\text{m s}^{-1}$ )
$g_s^c$	Canopy conductance ( $\text{m s}^{-1}$ )
$r_a$	Aerodynamic resistance ( $\text{s m}^{-1}$ )
$r_a^a$	Aerodynamic resistance between canopy source height and a reference level ( $\text{s m}^{-1}$ )
$r_a^s$	Aerodynamic resistance between the substrate and the canopy source height ( $\text{s m}^{-1}$ )

$r_a^c$	Bulk boundary layer resistance of the vegetation element in the canopy (s m <sup>-1</sup> )
$r_s^s$	Surface resistance of the canopy (s m <sup>-1</sup> );
$r_s^c$	Bulk stomatal resistance of the canopy (s m <sup>-1</sup> )

735

## 736 **Appendix B: Bayesian inference and the DREAM algorithm**

737 The posterior probability distribution of the parameter is calculated by Bayes' theorem:

$$738 \quad \pi(\boldsymbol{\theta} | D, M) = \frac{\pi(\boldsymbol{\theta} / M) p(D | \boldsymbol{\theta}, M)}{p(D | M)} \quad (\text{A1})$$

739 where  $\pi(\boldsymbol{\theta} / M)$  represents the prior density of  $\boldsymbol{\theta}$  under model  $M$ ;  $p(D | \boldsymbol{\theta}, M)$  is the joint likelihood of  
740 model  $M$  and its parameters  $\boldsymbol{\theta}$ ; and

$$741 \quad p(D | M) = \int p(D | \boldsymbol{\theta}, M) p(\boldsymbol{\theta} | M) d\boldsymbol{\theta} \quad (\text{A2})$$

742 is the marginal likelihood, or Bayesian model evidence (BME).

743 The likelihood function,  $p(D | \boldsymbol{\theta}, M)$ , used for parameter estimation, is specified according to the  
744 distributions of observation errors. Error  $e(t)$  in each observation  $D(t)$  at time  $t$  is expressed by

$$745 \quad e(t) = D(t) - f(t) \quad (\text{A3})$$

746 . Assuming  $e(t)$  follows a Gaussian distribution with a zero mean, and the likelihood function can be  
747 expressed as

$$748 \quad p(D | \boldsymbol{\theta}) = \prod_{t=1}^n \frac{1}{\sqrt{2\pi}\sigma} e^{-\frac{[e(t)]^2}{2\sigma^2}} \quad (\text{A4})$$

749 where  $n$  is the number of observations and  $\sigma$  represents the error variances.

750 In this study, we used the DREAM algorithm (Vrugt et al., 2008, 2009) to explore the ET models'

751 parameter space and to estimate BME. The DREAM sampling scheme is an adaptation of the global  
752 optimization algorithm of a shuffled complex evolution metropolis (SCEM-UA). This algorithm was  
753 described in more detail in Vrugt et al. (2008, 2009).

#### 754 **List of Tables**

755 **Table 1.** Prior distributions and parameter limits for the PM, SW, PT-FC and AA models. The values are  
756 derived from the literature.

757 **Table 2.** Maximum Likelihood Estimates (MLEs), Mean Estimates, 95% High-Probability Intervals  
758 (Lower Limit, Upper Limit).

759 **Table 3.** Slope and coefficient of determination ( $R^2$ ) of regression between measured and modeled  
760 half-hourly evapotranspiration values, and statistics of root mean square error (RMSE:  $W\ m^{-2}$ ), mean bias  
761 error (MBE:  $W\ m^{-2}$ ), index of agreement (IA), model efficiency (EF) and Logarithm of BME for the four  
762 ET models.

#### 763 **List of Figures**

764 **Figure 1.** Trace plots of the G-R statistic of Gelman and Rubin (Gelman and Rubin, 1992) using DREAM  
765 for the PM model (a) and (b) the SW model. Different parameters are coded with different colors. The  
766 dashed line denotes the default threshold used to diagnose convergence to a limiting distribution.

767 **Figure 2.** (a)-(e), (f)-(l), (m)-(n), and (o)-(p) show histograms for the PM (black), SW (cyan), PT-FC  
768 (magenta) and AA (orange) models, respectively. These histograms are constructed from all chains for each  
769 model and a total of  $40,000 \times N$  realizations are simulated using DREAM. The  $x$  axes represent the  
770 prespecified limits of the parameters.

771 **Figure 3.** Regressions between measured and modeled half-hourly ET values produced by different  
772 models from DOY 154 to DOY 270: (a) PM, (b) SW, (c) PT-FC and (d) AA. The regressions are:  $Y =$   
773  $0.99X$  ( $R^2 = 0.76$ ),  $Y = 1.05X$  ( $R^2 = 0.82$ ),  $Y = 0.91X$  ( $R^2 = 0.75$ ), and  $Y = 0.92X$  ( $R^2 = 0.75$ ) for the PM,  
774 SW, PT-FC and AA models, respectively.

775 **Figure 4.** Mean bias error (MBE) of predicted and observed ET values for (a) PM, (b) SW, (c) PT-FC and  
776 (d) AA models from DOY 154 to DOY 270. Parameters used for prediction are estimated by DREAM with  
777 the dataset for the calibration period from DOY 154 to DOY 202.

778 **Figure 5.** Variation of the mean posterior expectation of the potential  $y_k$  with  $\beta_k$  for the PM, SW, PT-FC  
779 and AA models. The nits denote natural log units.

780

781 **Table 1** Prior distributions and parameter limits for the PM, SW, PT-FC and AA models. The values are  
782 derived from the literature.

Parameter	Description	Prior range PM		Prior for SW		Prior for PT and AA		References
		Lower	upper	Lower	upper	Lower	upper	
$g_{max}$ (mm s <sup>-1</sup> )	maximum stomatal conductance	0	50	0	50			Kelliher et al. (1995)
$Q_{50}$ (W m <sup>-2</sup> )	visible radiation flux	10	50	10	50			Leuning et al. (2008)
$D_{50}$ (kPa)	vapor pressure deficit	0.5	3	0.5	3			Leuning et al. (2008)
$K_q$	extinction coefficient	0	1	0	1			Leuning et al. (2008)
$K_a$	extinction coefficient	0	1	0	1			Leuning et al. (2008)
$b_1$ (s m <sup>-1</sup> )	empirical constant			4.5	11.3			Sellers et al. (1992)
$b_2$ (s m <sup>-1</sup> )	empirical constant			0	8			Sellers et al. (1992)
$\beta_1$	empirical constant					0.5	1.5	Flint et al. (1991);
$\beta_2$	empirical constant					0.1	10	Barton. (1979)

783

784 **Table 2** Maximum Likelihood Estimates (MLEs), Mean Estimates, 95% High-Probability Intervals  
785 (Lower Limit, Upper Limit).

Parameter	Posterior for PM			Posterior for SW			Posterior for PT and AA		
	MLE	Mean	CI	MLE	Mean	CI	MLE	Mean	CI
$g_{max}$ (mm s <sup>-1</sup> )	0.04	0.04	(0.03, 0.04)	0.01	0.01	(0.005, 0.012)			
$Q_{50}$ (W m <sup>-2</sup> )	49.96	48.52	(39.73, 49.74)	47.49	40.32	(11.02, 48.99)			
$D_{50}$ (kPa)	3.00	2.87	(1.92, 2.97)	2.98	2.88	(2.26, 2.98)			
$K_q$	1.00	0.99	(0.911, 0.998)	0.99	0.88	(0.06, 0.98)			
$K_a$	1.00	0.98	(0.822, 0.995)	0.12	0.12	(0.074, 0.184)			
$b_1$ (s m <sup>-1</sup> )				4.51	4.57	(4.52, 4.96)			
$b_2$ (s m <sup>-1</sup> )				0.39	0.57	(0.07, 1.38)			
$\beta_1$							1.1 <sup>a</sup>	1.098 <sup>a</sup>	(1.06, 1.16) <sup>a</sup>
							1.5 <sup>b</sup>	1.499 <sup>b</sup>	(1.492, 1.499) <sup>b</sup>

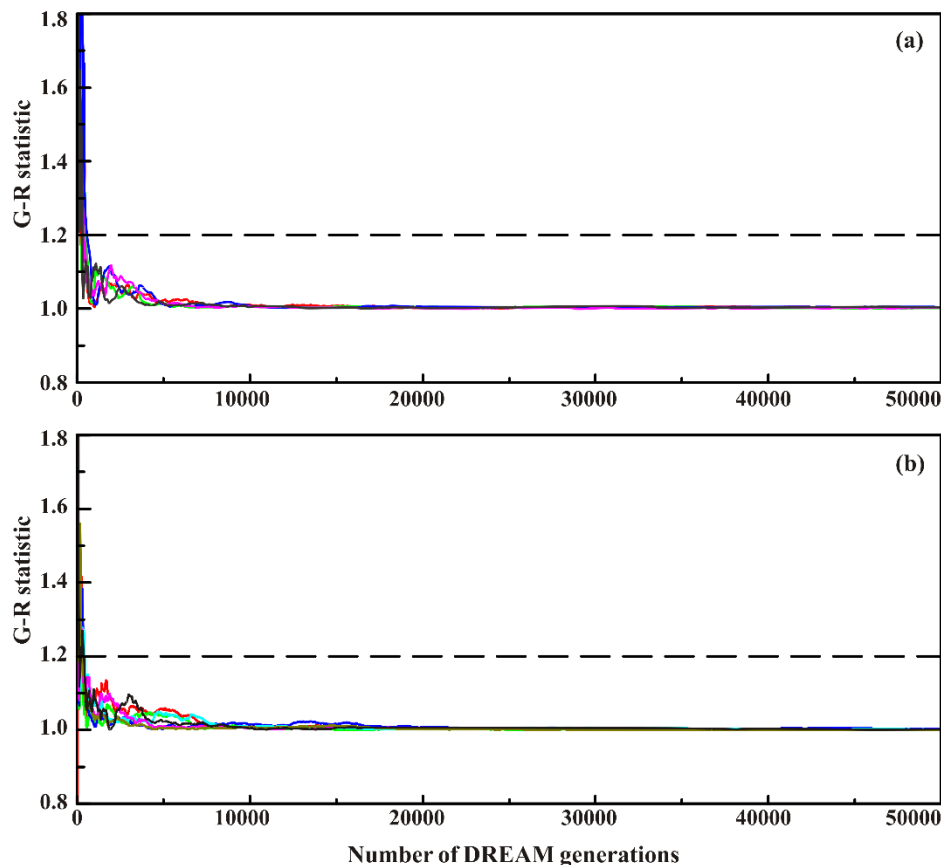
$\beta_2$	10.00 <sup>a</sup>	9.75 <sup>a</sup>	(7.97, 9.95) <sup>a</sup>
	10.00 <sup>b</sup>	9.94 <sup>b</sup>	(9.44, 9.99) <sup>b</sup>

786 <sup>a</sup> PT-FC model; <sup>b</sup> AA model.

787 **Table 3** Slope and coefficient of determination ( $R^2$ ) of regression between measured and modeled  
 788 half-hourly evapotranspiration values, and statistics of root mean square error (RMSE:  $W m^{-2}$ ), mean bias  
 789 error (MBE:  $W m^{-2}$ ), index of agreement (IA), model efficiency (EF) and Logarithm of BME for the four  
 790 ET models.

Model	Slope	$R^2$	RMSE	MBE	IA	EF	BME
PM	1.01	0.76	85.38	-9.52	0.93	0.74	-6300.5
SW	1.05	0.82	76.34	-19.07	0.95	0.79	-6025.1
PT-FC	0.91	0.75	94.39	25.42	0.92	0.68	-6366.8
AA	0.92	0.75	95.09	23.29	0.92	0.67	-6390.3

791

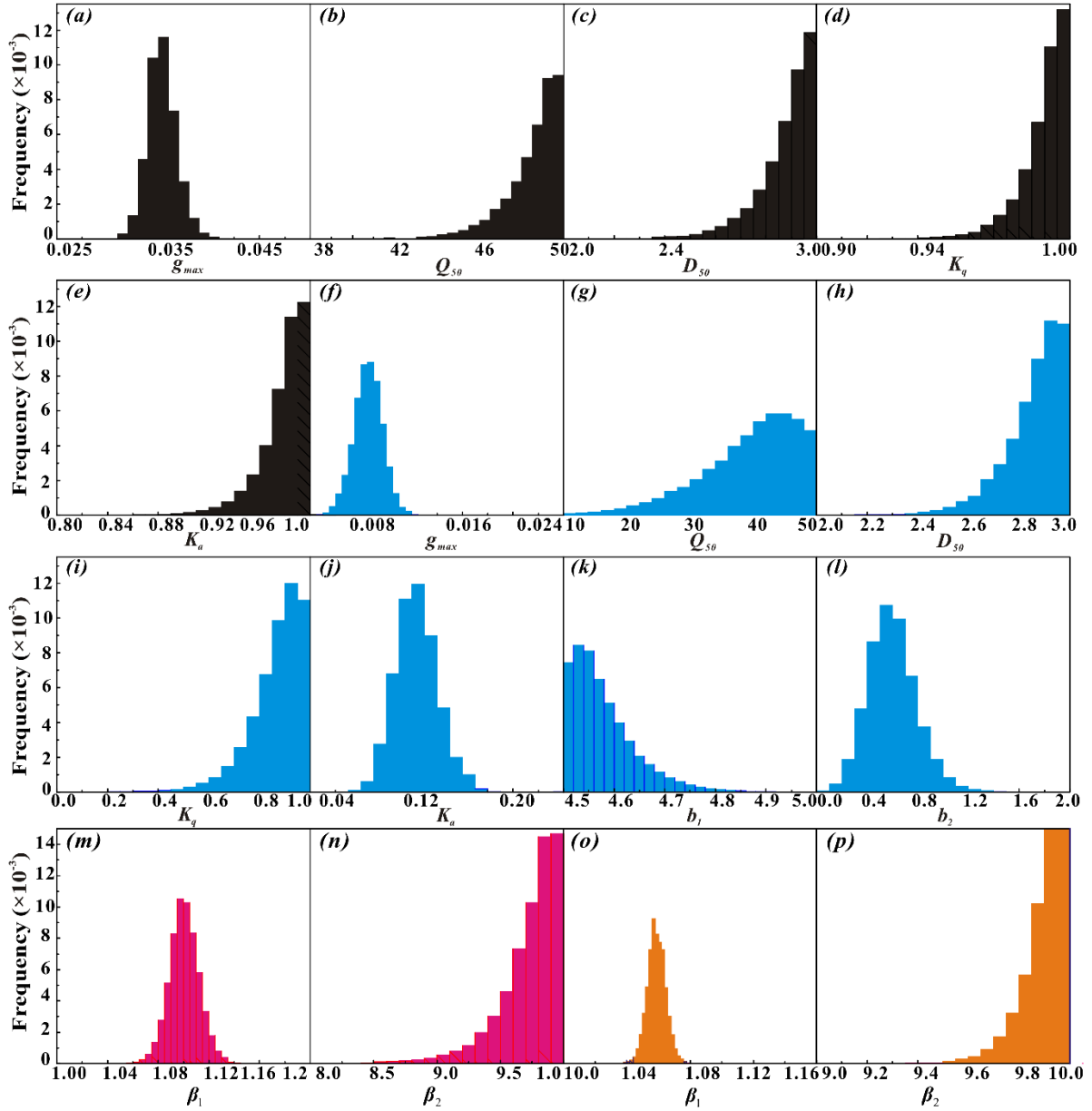


792

793 **Figure 1** Trace plots of the G-R statistic of Gelman and Rubin (Gelman and Rubin, 1992) using DREAM  
 794 for the PM model (a) and (b) the SW model. Different parameters are coded with different colors. The  
 795 dashed line denotes the default threshold used to diagnose convergence to a limiting distribution.

796

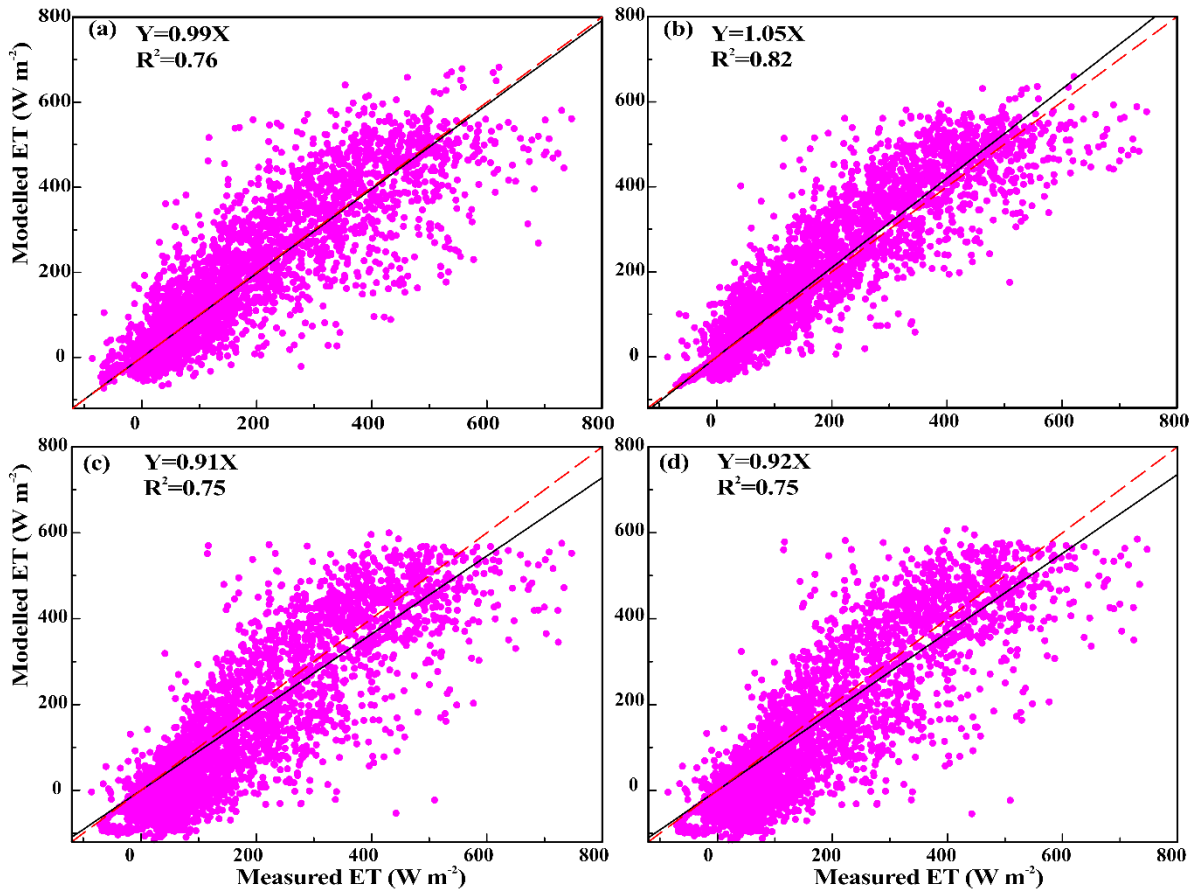
797



798

799 **Figure 2** (a)-(e), (f)-(l), (m)-(n), and (o)-(p) show histograms for the PM (black), SW (cyan), PT-FC  
 800 (magenta) and AA (orange) models, respectively. These histograms are constructed from all chains for each  
 801 model and a total of  $40,000 \times N$  realizations are simulated using DREAM. The  $x$  axes represent the  
 802 prespecified limits of the parameters.

803

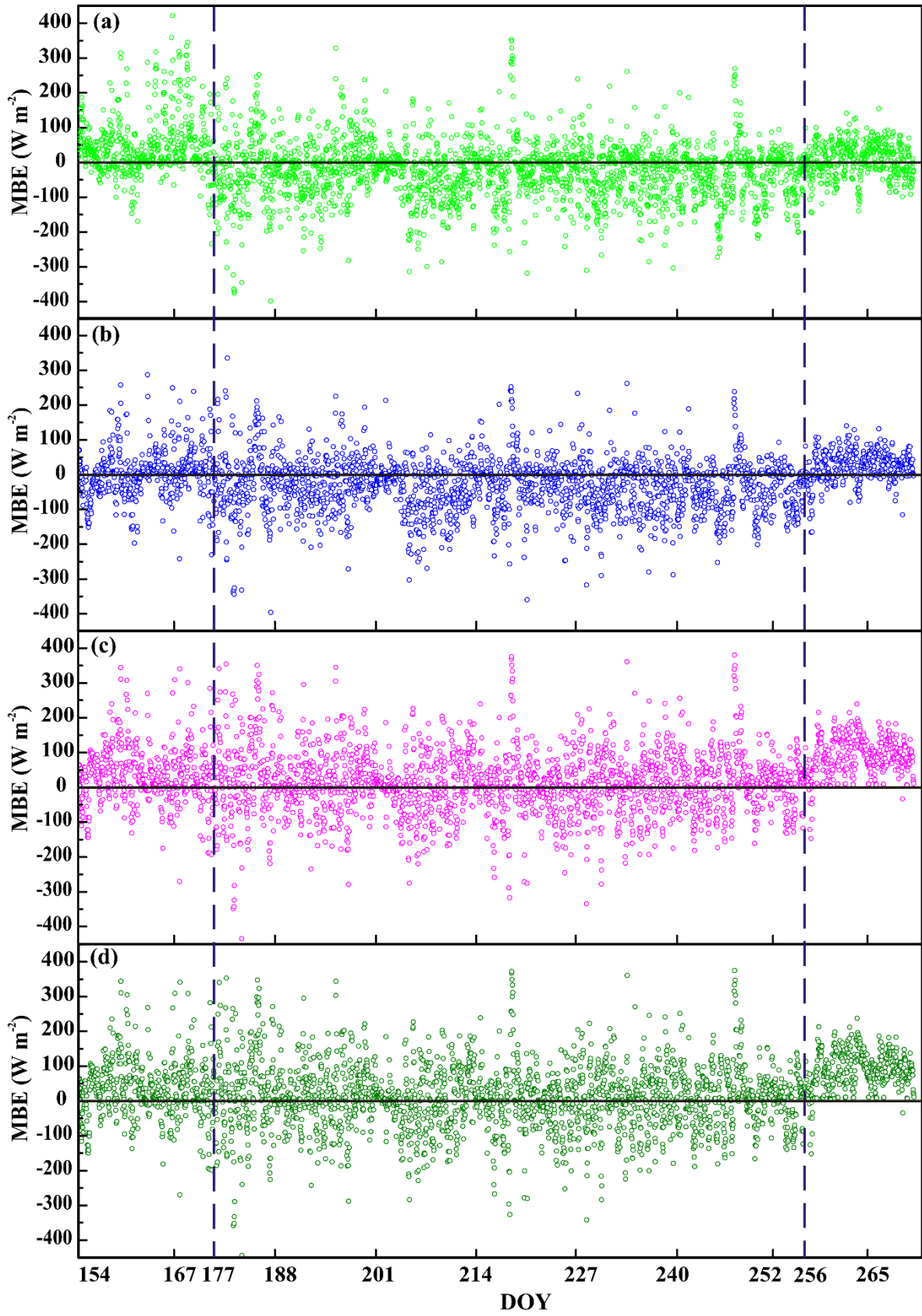


804

805 **Figure 3** Regressions between measured and modeled half-hourly ET values produced by different models  
 806 from DOY 154 to DOY 270: (a) PM, (b) SW, (c) PT-FC and (d) AA. The regressions are:  $Y = 0.99X$  ( $R^2 =$   
 807  $0.76$ ),  $Y = 1.05X$  ( $R^2 = 0.82$ ),  $Y = 0.91X$  ( $R^2 = 0.75$ ), and  $Y = 0.92X$  ( $R^2 = 0.75$ ) for the PM, SW, PT-FC  
 808 and AA models, respectively.

809



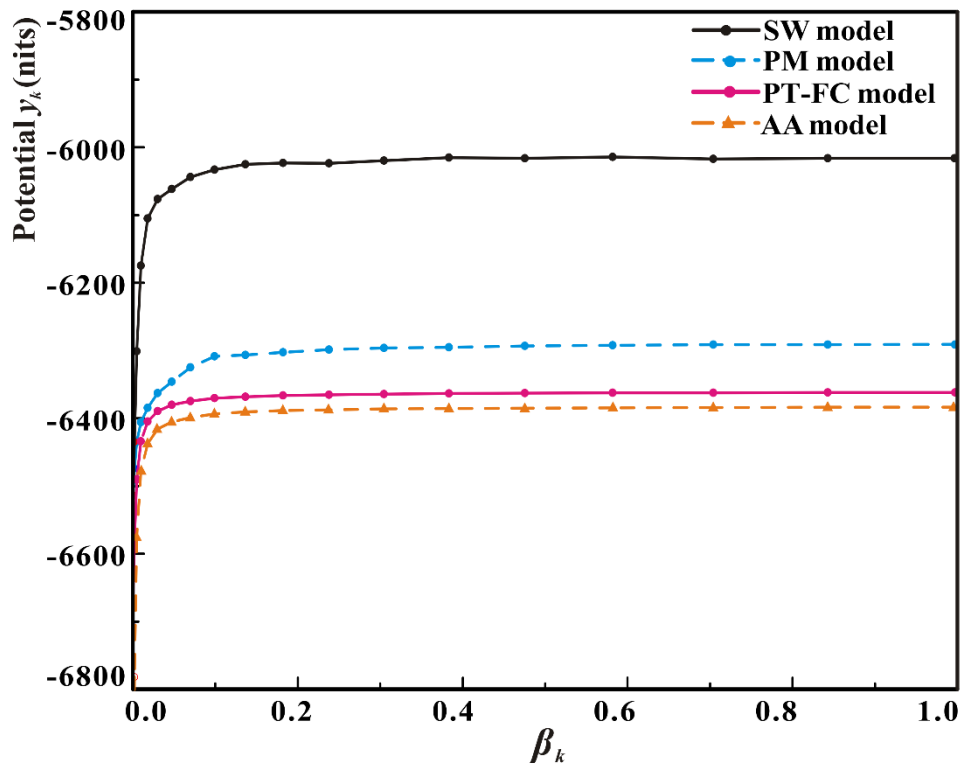


810

811 **Figure 4** Mean bias error (MBE) of predicted and observed ET values for (a) PM, (b) SW, (c) PT-FC and  
 812 (d) AA models from DOY 154 to DOY 270. Parameters used for prediction are estimated by DREAM with

813 the dataset for the calibration period from DOY 154 to DOY 202.

814



815

816 **Figure 5** Variation of the mean posterior expectation of the potential  $y_k$  with  $\beta_k$  for the PM, SW, PT-FC and  
817 AA models. The nits denote natural log units.

818